Ipadeola *et al. Energy Mater* 2024;4:400079
DOI: 10.20517/energymater.2024.34

Energy Materials

Review

Open Access

Recent advances in porous multimetallic alloy-based anodes for rechargeable alkali metal-ion batteries

Adewale K. Ipadeola[1,2], Aboubakr M. Abdullah[1,*], Kamel Eid[2,*]

[1]Center for Advanced Materials, Qatar University, Doha 2713, Qatar.
[2]Gas Processing Center (GPC), College of Engineering, Qatar University, Doha 2713, Qatar.

***Correspondence to:** Dr. Aboubakr M. Abdullah, Center for Advanced Materials, Qatar University, Doha 2713, Qatar. E-mail: bakr@qu.edu.qa; Dr. Kamel Eid, Gas Processing Center (GPC), College of Engineering, Qatar University, Doha 2713, Qatar. E-mail: kamel.eid@qu.edu.qa

How to cite this article: Ipadeola AK, Abdullah AM, Eid K. Recent advances in porous multimetallic alloy-based anodes for rechargeable alkali metal-ion batteries. *Energy Mater* 2024;4:400079. https://dx.doi.org/10.20517/energymater.2024.34

Received: 22 Apr 2024 **First Decision:** 12 Jun 2024 **Revised:** 29 Jun 2024 **Accepted:** 16 Jul 2024 **Published:** 8 Nov 2024

Academic Editor: Jiazhao Wang **Copy Editor:** Fangyuan Liu **Production Editor:** Fangyuan Liu

Abstract

The rechargeable alkali metal-ion batteries (RAMIBs) are highly promising candidates for next-generation efficient energy storage devices, owing to their outstanding theoretical specific capacities and extremely low electrochemical potentials. However, RAMIBs possess unsuitable lifespans, low mechanical durability and inevitable side reactions attributable to their inherent severe volumetric/structure alteration during the charge-discharge cycles. These hitches could be solved using porous multimetallic alloy-based anodes, due to their impressive specific capacities, low working potential, low cost, and earth-abundance, which can meet sustainability and practical application needs. Meanwhile, great surface area, electrical conductivity, structural stability, and ability to accommodate the generated alkali metal ions can yield satisfactory coulomb efficiency and long durability. Immense efforts are dedicated to rationally designing porous multimetallic alloy-based anodes for RAMIBs, so it is essential to provide timely updates on this research area. Herein, we reviewed recent advances in porous multimetallic alloy-based anodes (i.e., Sn, Mn, Mo, Co, V, and Fe) for RAMIBs (i.e., lithium-ion batteries, sodium-ion batteries, and potassium-ion batteries. This is rooted in the engineering approaches (i.e., template-based, hydrothermal/solvothermal, chemical reduction, electrochemical deposition, sol-gel, and electrospinning) to fundamental insights (i.e., mechanisms, key parameters, and calculations) and precise evaluation for structural changes, and mechanisms by various experimental, theoretical, and *in-situ* analysis to optimizing their performance. Also, advances in RAMIBs recycling and circular economy were discussed. Eventually, we highlighted the current drawbacks and provided proposed perspectives to solve these issues and enable practical utilization of such anodes for large-scale applications.

Keywords: Alkali metal-ion batteries, porous multimetalllic alloy-based anodes, lithium-ion, sodium-ion, and potassium-ion batteries, battery recycle

INTRODUCTION

There are global concerns regarding environmental threats (i.e., global warming) and nonrenewable fossil fuel exhaustion, which raise the need for gas conversion reactions[1,2] and developing green energy sources[3-8]. Lithium-ion batteries (LIBs) with their trustworthy power source are the most common and efficient energy storage devices widely used in various portable devices and electric cars, but the high cost and earth-rarity of Li are crucial issues in the sustainable future[9-12]. The efficiency and performance of LIBs are shaped by the anode (i.e., shape and composition) and electrolytes[11-13]. Rechargeable alkali metal-ion batteries (RAMIBs) emerged as a promising alternative to traditional Li-batteries, owing to their tolerable cost, reliable theoretical specific capacities (Li = 3,860 mAh/g; Na = 1,166 mAh/g; K = 685 mAh/g), and low electrochemical redox voltage [i.e., Li = 3.04 V, Na = 2.71 V, and K = 2.93 V *vs.* Standard Hydrogen Electrode (SHE)][14]. However, the alkali metal-ion batteries are still not up to the level of commercial scale, owing to their viability to dendrite growth, repetitive breakage or regeneration of the solid electrolyte interphase, causing subsequent unreliable safety, low energy efficiency, and low durability. Immense efforts devoted to solving these barriers lie in the development of controlled size, composition, and morphology of the anodes, new electrolytes (i.e., ether-based electrolytes, solid-state electrolytes, and multifunctional electrolyte additives), and the design of new hierarchical supports[10,15-18]. These solutions led to decreasing the local current density, controlling alkali-metal deposition, enhancing mechanical properties, increasing the ionic conductivity, ceasing dendrite growth, and stabilizing alkali metal anodes from corrosion. However, the intrinsically great activity of alkali metals and the significant volume alteration during plating or stripping are critical barriers for practical applications of RAMIBs[19,20].

Another promising solution is the rational formation of porous multimetallic alloy-based anodes (PMMAs), especially porous transition metals, which are the most promising to solve the current hitches in RAMIBs, owing to their impressive specific capacities and low working voltage[16,21,22]. This is in addition to the low cost and abundance of transition metals, which can meet the requirements of both sustainability and practical application[23,24]. Moreover, PMMA anodes act as a protective layer, which enhances the cyclic durability, rate capability, and plating/stripping Coulombic efficiency (CE) of RAMIBs[25]. Besides, PMMAs are endowed with enhanced specific capacity (SC), alkaline metal (Li^+/Na^+/K^+) ion diffusion/kinetics, stable architectural integrity, negligible volume expansion and pulverization in RAMIBs, compared to their monometallic analogous[26,27]. Notably, using at least one alkali metal with PMMAs decreases the high reactivity of alkali metal, provides abundant channels for quick ion transfer, and acts as mechanical supports, hence preferring quick and orderly metal plating and stripping[23]. Additionally, direct use of PMMAs with their interphases can plausibly serve as an artificially protective layer to tailor the ion flux, increase rapid ion diffusion, and inhibit the side reactions between the electrolyte and electrode. This has led to an exponential increase in publications (i.e., 100 articles, cited ~1,500 times) [Figure 1A], with much attention on the rational design of PMMAs for alkali metal-ion batteries; hence, it is important to provide timely updates on this research area. Although there are various recent excellent reviews on alkali metal batteries and metal anodes [Supplementary Table 1], the PMMA anodes for LIBs, sodium-ion batteries (SIBs), and potassium-ion batteries (PIBs) have not yet been reviewed to the best of our knowledge[14,27,28].

This review summarized the progress in the fabrication methods (i.e., template-based, hydrothermal/solvothermal, chemical reduction, electrochemical deposition, sol-gel, and electrospinning) of PMMAs (i.e., Sn, Mn, Mo, Co, V, and Fe) for RAMIBs (i.e., LIBs, SIBs, and PIBs) [Figure 1B]. These are classified and grouped according to the active atoms/elements in their compositions, whose physicochemical merits and electrochemical performance are robustly discussed in detail. This is in addition

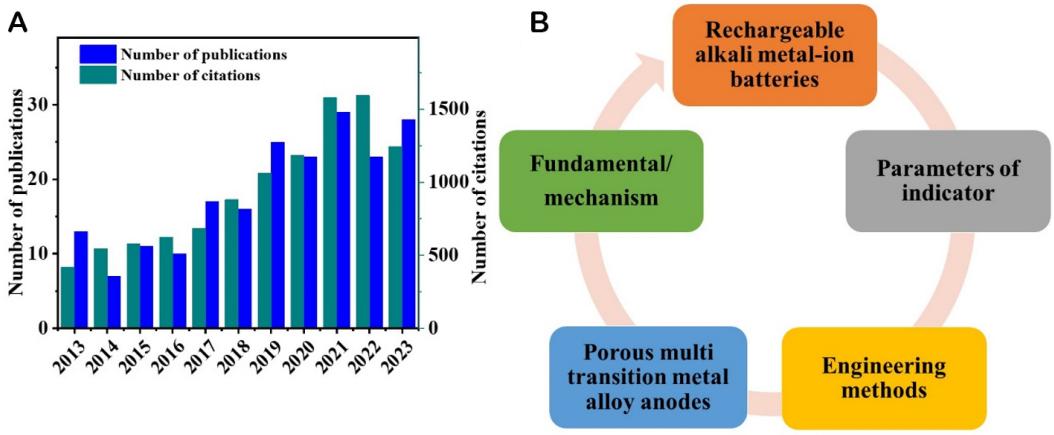

Figure 1. (A) Database literature survey using keywords "multimetallic alloy anodes for batteries" according to the "Web of Science" and (B) review focus.

to the fundamental issues (i.e., mechanisms, key parameters, and calculations) of such batteries, along with deep discussions on the key descriptors of these batteries (i.e., lifespans, energy density (ED), structural changes, and mechanisms). A lot of experimental data, theoretical simulations, and *in-situ* analysis were provided to optimize the performance of PMMAs in LIBs, SIBs, and PIBs. Meanwhile, a conclusion and perspectives/outlooks are provided to underline the current challenges and propose solutions for such anodes and batteries.

FUNDAMENTAL AND MECHANISMS OF RECHARGEABLE ALKALI-ION BATTERIES

The RAMIBs, including LIBs, SIBs and PIBs, comprise four basic parts: anodes, cathodes, electrolytes and separators. The electrodes (anodes and cathodes) are good electrical conductors, while electrolyte functions as an ionic conductor, as briefly explained below.

• Anode: This is a negative electrode (metal or alloy) where negatively charged ions migrate.

• Cathode: This is a positive electrode (layered structure of metallic oxide, sulfides, and/or carbon materials) where positively charged ions migrate.

• Electrolyte: This is a solution containing dissociated salts that allows the movement of ions between the anode and cathode.

• Separator: This is a permeable or porous membrane that keeps the anode and cathode apart to eschew electrical short circuits but allows the movement of ionic charge carriers required for the passage of current in the battery.

The anode and cathode are often made up of different conducting materials, kept apart by the separator and immersed in the electrolyte solution. A typical RAMIB is shown in Figure 2 with similar mechanisms. For example, in LIBs, charging and discharging ensues via the movement of A^+-ions between the cathode and anode, coupled with exchange of electrons (e^-s). Particularly, the charging Li/Na/K is delithiated/desodiated/depotassiated from the cathode (i.e., Li-based compound) and the interlayer anode [i.e., metal alloys (MAs) or carbon] are lithiated/sodiated/potassiated with Li/Na/K, and vice-versa during the discharge process, as given in Eqs. 1 and 2, where A represents Li^+ or Na^+ or K^+ ions and MAs are metal alloys.

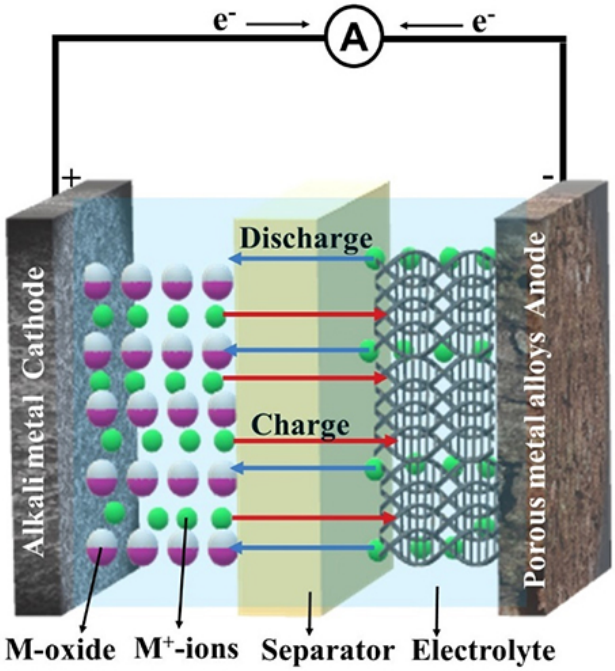

Figure 2. Schematic illustration of rechargeable alkali metal-ion battery.

$$\text{Initial charge: } ACoO_2 + C \rightarrow A_{1-x}CoO_2 + A_xMA \quad (1)$$

$$\text{Discharge: } A_{1-x}CoO_2 + A_xC \rightarrow A_{1-x-dx}CoO_2 + A_{x-dx}MA \quad (2)$$

Parameters of indicator and calculations

In addition to the materials' cost, toxicity and safety of the components of RAMIBs, their performance can be assessed by various parameters of indicators, including cell voltage, C-rate, SC, capacity retention (CR), ED, power density, CE, voltage efficiency and energy efficiency, which aid in the rational design and fabrication of suitable intercalation electrodes for high ED batteries[29-31]. These are briefly discussed below:

• Cell voltage: This is the driving force for the movement of alkali metal ions and electrons from one electrode to the other. Thermodynamically, it is the electrochemical potential difference, which is proportional to Gibb's free energy (ΔG), as given in

$$\Delta G = -nFV \quad (3)$$

Here, n represents the total number of electrons, Faraday's constant F = 96,485.3 (C/mol), and V refers to the cell voltage.

Discharge rate or C-rate: This is the rate at which a battery is discharged/charged in relation to its capacity. For instance, 1C-rate indicates that a battery is fully discharged in 60 min (1 h), and 10 Ah capacity of a battery gives a 1C-rate equivalent to 10 A.

• Specific capacity (SC): This is the amount of electrons intercalated/deintercalated per unit mass of the electrode during cycling. The SC is reported with mass or volume of an active electrode, called gravimetric

SC (GSC, mAh/g) or volumetric SC (VSC, mAh/cm^3), respectively, and calculated using

$$\mathrm{SC} = \frac{nF}{3600\,M} \tag{4}$$

Here, the number of available sites for active Mn^+ ions intercalated into the host matrix of the battery's capacity. Also, the storage capacity can be measured with respect to unit area, called areal capacity (mAh/cm^2). The VSC is particularly crucial when designing batteries for high energy applications, such as electric vehicles and grid storage.

• Capacity retention (CR, cyclability/stability): This is the number of times a battery can be discharged/charged at both fixed and various current densities. For practical application in industries, a good battery should retain at least 80% of its initial SC after multiple cycles (charged/discharged).

• Energy density (ED): This is the overall energy stored in a battery, which is calculated by multiplying the working voltage (V) and reversible capacity (C), as given in

$$E = V \times C = V \times \mathrm{i} \times t \tag{5}$$

Here, i indicates the current, and t represents time. Electrodes having higher potential (voltage), which is a function of the amount of alkali metal ion intercalated, and layered structure with various compositions facilitate higher ED. The ED can be expressed as gravimetric (Wh/kg) or volumetric (Wh/L).

• Power density: This is the optimal power delivered by a battery with regard to its electrode mass or volume. It shows how fast work is done with the availed energy in the battery, as given in

$$P = (i \times V) = (i^2 \times R_{\mathrm{int}}) \tag{6}$$

Here, i, V, and R_{int} denote the current, voltage, and internal resistance, respectively. The R_{int} is a function of ionic conductivity of the alkali metal ions, electrical conductivity of electrodes and reaction kinetics during cycling. The power density can be reported per unit mass [i.e., gravimetric power density (W/kg)] or unit volume [i.e., volumetric power density (W/L)]. Surface reactivity, conductivity, surface morphology, electrochemical, chemical and structural stability of electrodes are the contributory factors for optimized power density.

• Coulombic efficiency (CE): This is the ratio of energy withdrawn from a battery during discharge and energy restored during charging, as given in

$$\mathrm{CE} = \frac{\text{Specific capacity of discharging}}{\text{Specific capacity of charging}} \times 100 \tag{7}$$

A good battery should have close to 100% CE.

• Voltage/voltaic efficiency: This is the ratio of mean discharging voltage to charging voltage. High active surface area and electrical conductivity of electrodes enable increased voltage efficiency.

• Energy efficiency: This is the ratio of energy densities during discharge and charge process.

The cyclability, ED, power density, and rate capability are dependent on the ionic and electrical conductivities of the electrodes. Hence, a battery must maintain low internal resistance and higher conductivities to obtain excellent performance. Meanwhile, low molar mass electrodes enable higher capacity and rate capability.

ENGINEERING METHODS FOR POROUS MULTIMETALLIC ALLOY-BASED ANODES

The PMMA anodes are controllably synthesized by various methods, including template-based, hydrothermal/solvothermal, chemical reduction, electrodeposition, sol-gel, co-precipitations and electrospinning.

Template-based methods

The PMMAs are mostly and best prepared via the template-based methods, i.e., hard-templates or soft-templates[3,27]. The hard-template is appropriate to tailor the preparation of well-ordered PMMAs, initiated by the infiltration of metal precursors into the template by co-deposition or *in-situ* deposition or self-assembly, and then removal of the template by etching (i.e., NaOH or HF) and/or heating, thereby replicating the exact porosity of the template. Zeolites, mesoporous silica (i.e., MCM-41, MCM-48, KIT-6 and SA-15), alumina membranes and colloidal crystals [i.e., crystal latex, salt-like (KCl)] are typical examples of the hard-templates[3,27], for the preparation of nanotube-like PMMAs [Figure 3A]. Similarly, soft-templates utilize lyotropic liquid crystals, such as block copolymers (i.e., 3,4-dihydroxy-D-phenylalanine, 3,4-dihydroxy-L-phenylalanine, and (R)-phenylethanol), surfactants (Brij® C10, polyvinylpyrrolidone, and pluronic F127), degradable copolymers [i.e., polystyrene-*block*-poly(4-vinylpyridine), polystyrene-*b*-poly(l-lactide), poly(lactic-co-glycolic acid), and polyisoprene-*block*-polystyrene-*block*-poly(propylene carbonate)] and micelle assembly (PS-*b*-P4VP micelles)[27,32]. A typical example of the soft-template method for the synthesis of PMMAs is presented in Figure 3B. Despite the advantages of template methods for the preparation of PMMAs, there is volume collapse during the metal precursors' reduction and incomplete retention of template shapes and porosity after their removal, which pose a challenge for controlling the morphologies, particularly for powder or film nanostructures on non-conductive substrates. This hitch is often surmounted by combining the template methods with chemical reduction or electrodeposition. This method is often used for the synthesis of PMMA anodes for RAMIBs. These methods utilize the dynamic structures of templates to control the morphologies, porosity, surface area and other physicochemical features of the PMMA anodes.

Hydrothermal/solvothermal method

The synthesis of PMMAs using hydrothermal methods involves the mixing of aqueous metal precursors (i.e., acetate, chloride, nitrate and hydroxide dissolution in water), where a pH modular/additive (i.e., KI, KBr or KOH) serves as a catalyst when magnetically stirred or ultrasonicated, and surfactants (i.e., polyvinylpyrrolidone (PVP), pluronic F127) as structure-directing agents[33,34]. The aqueous solution is sealed in an autoclave and heated at elevated temperature for some time (2-24 h), and then the anticipated product is washed by centrifugation for several cycles and dried in a vacuum oven, prior to calcination [Figure 4A]. Solvothermal method is similar to hydrothermal method, but it uses non-aqueous solvents, such as dimethylformamide, ethylene glycol, isopropanol, ethanol, and butanol, which may act as a structure-directing agent. The fabrication methods of the PMMAs via hydrothermal/solvothermal method entails initial nucleation and subsequently direct attachment growth; meanwhile, the surfactant is adsorbed or interacts with the anion additives (Br^-, I^-, OH^-) and sometimes *in-situ* etching-induced porous architectures[35-37]. The hydrothermal/solvothermal method is easy, effective and appropriate for the

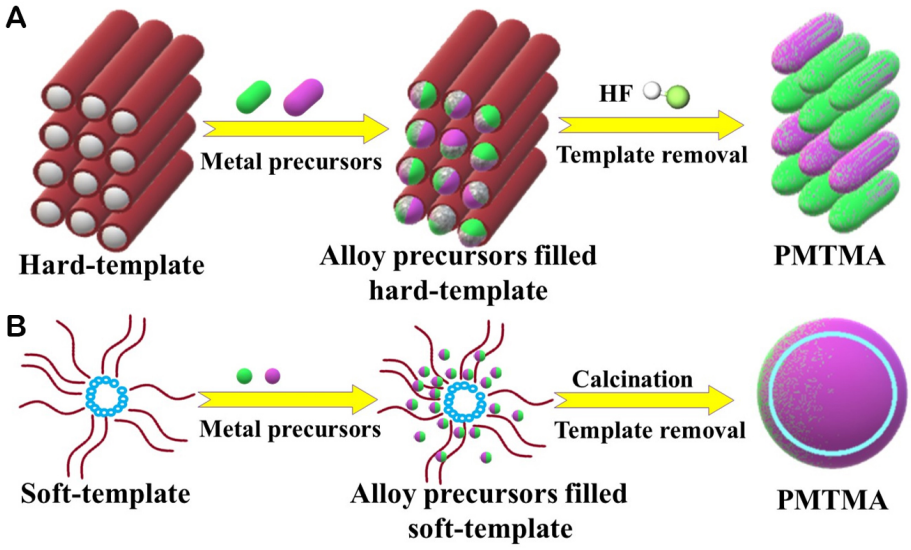

Figure 3. Schemes of (A) hard-template and (B) soft-template methods of preparing PMMAs.

Figure 4. Scheme of (A) hydrothermal/solvothermal and calcination, and (B) chemical reduction for the synthesis of PMMAs.

preparation of PMMAs, their oxides, chalcogenides, spinels, perovskites, high entropy alloys, and composites, with or without supports [i.e., carbon, nickel foam (NF)] in various architectures (nanospheres, nanocubes, nanosponges, nanocages, flower-like architectures, *etc.*).

Chemical reduction method

The chemical reduction method uses suitable reducing agents, such as $NaBH_4$, ascorbic acid, PVP, *etc.*[38-40]. The formation mechanism of the PMMAs follows a burst nucleation of metal with high standard reduction potential, which eventually serve as seeds for other metal(s) atoms to form multiple crystallites with large surface-free energy; then, these crystallites aggregate and undergo continuous direct-attachment/diffusion-limited growth across the interface through Brownian motion [Figure 4B][41]. At rapid reduction rate, the as-formed nuclei grow along the single-crystalline lines to yield polyhedron shapes (i.e., cubes, tetrahedrons, and octahedrons) with O_h and T_d symmetry. In contrast, slow reduction rate affords a five-fold twinned nuclei growth into polyhedrons with I_h symmetry (dodecahedrons and icosahedrons). Also, the structures of the PMMAs are a function of the adsorption model of the structure-directing agents[42], including ionic polymers [i.e., cetyltrimethylammonium bromide (CTAB) and cetyltrimethylammonium chloride (CTAC)]

and non-ionic polymers (i.e., Pluronic F127, Brig-58, and PVP), on the as-formed nuclei with the respective functional groups. This then leads to self-assembly to yield micelles that serve as *in-situ* templates during the growth for the formation of porous wire-like, branched and 3D nanocrystals.

Electrochemical deposition method

The preparation of PMMAs via electrochemical deposition is low-cost, rapid, single-step and low energy-intensive (i.e., low potential and room temperature) in the form of thin films, coatings and various shapes/compositions. The fabrication process involves reduction/oxidation of metal ions in an electrolyte (acid, neutral or alkaline), which are deposited on the conductive materials when certain potential is applied, utilizing a 3-electrode configuration, comprising the counter electrode (i.e., Pt wire and graphite), reference electrode (i.e., Ag/AgCl, and SCE) and working electrode (i.e., glassy carbon, carbon paper, carbon cloth sheet) [Figure 5A]. The modulation of the shapes and compositions of the PMMAs are functions of the electrolyte types, applied potential, cell set-up and deposition time. This method is easy and could be combined with other approaches for the synthesis of thin film; however, it requires a lot of precaution and skills for controlled morphologies and compositions.

Sol-gel method

Controlled texture, size and surface features of PMMAs in the form of aerogels, xerogels or cryogels are prepared via sol-gel method, which is cost-effective, easy to implement, and provides high quality and large yield[43,44]. The fabrication process of PMMAs through this method follows several steps: hydrolysis, condensation, aging & drying and crystallization [Figure 5B][45]. Hydrolysis involves the mixing of metal alkoxide precursors and solvent, where the nucleophilic oxygen of water attaches to the metal alkoxide to remove it from the formation of the alcohol functional group (M-OH). This is affected by several parameters [nature of R-group, alkoxy functional group steric hindrance, temperature, pH, aqueous or non-aqueous solvents, ratio of solvent to metal alkoxide, and the amounts of catalysts (acid or base)]. These parameters can sometimes make it difficult to control the synthesis and the structure of the obtained gel depending on the catalyst, owing to the rate of hydrolysis. The hydrolysis rate is often faster in alkaline media than in acidic media[46]. The condensation is the formation of a polymer network, composed of metal oxide linkages, due to the removal of solvent (water or alcohol) to form a sol. This step raises the solution's viscosity during the polymer network growth and forms a porous structure within the gel-phase. Aging is the continuous polycondensation within the solution and precipitation of the gel network, which lowers porosity, but increases thickness of the colloidal nanoparticles. Drying is the evaporation during gelation, whose rate significantly affects the gel structure. The network structure of the gel may be affected by liquids removal: if the structure is retained, an aerogel (high pore volume and surface area) is formed; if it collapses, a xerogel (low pore volume and surface area) is formed; but it is removed at low temperature, a cryogel is formed. The drying of gel requires heat treatment to remove surface OH groups and compress to form crystalline PMMAs[47].

Electrospinning method

The electrospinning is a useful and worthwhile technology for the preparation of 1D nanofibrous materials for nanotechnological applications in biomedicine, fuel cells, energy storage, electronics, and sensors[48,49]. This method involves four main components: a high-voltage power supply, a syringe pump, a spinneret (i.e., a hypodermic needle with a blunt tip) and a conductor collector[50]. It utilizes an electrodynamic process to electrify liquid droplets of metal precursors to produce a jet that is then stretched and elongated to give PMMA nanofibers [Figure 5C]. The fabrication mechanism involves the extrusion of metal precursor liquid from a spinneret to afford a suspended droplet, due to the surface tension; then, the electrostatic repulsion of the surface charges of the same sign deforms the droplet into a Taylor cone, where a charged jet is ejected. The jet is extended initially in a straight line, then subjected to vigorous whipping

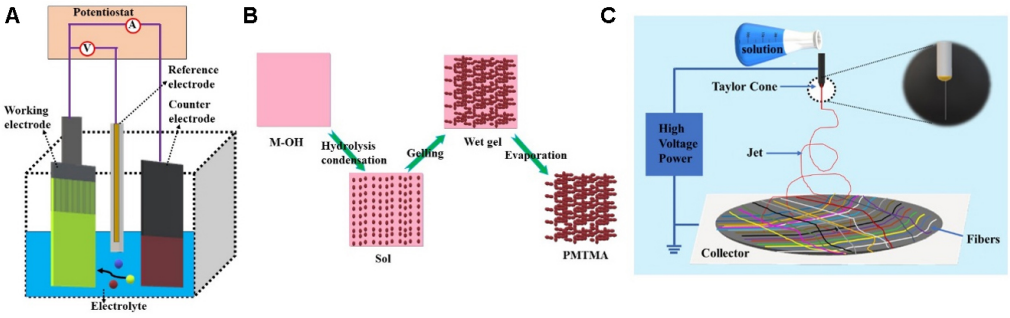

Figure 5. The illustration of (A) electrodeposition, (B) sol-gel and (C) electrospinning methods for the preparation of PMMAs.

motions, owing to bending instabilities, stretches to finer diameters, and solidifies rapidly, resulting in deposition of solid porous PMMA nanofibers on the conductor substrate[51,52].

ALKALI METAL-ION BATTERIES

Lithium-ion batteries

In the last decade, numerous studies have explored the use of MA anodes for rechargeable Lithium-ion batteries (LIBs). Nevertheless, research on PMMA anodes has been relatively limited. PMMA anodes are considered preferable because of their superior specific capacities relative to carbon anodes. However, during cycling, these anodes are conspired with large capacity irreversibility at the 1st cycle and meager cycling performance, owing to volume variation. These hiccups are being surmounted by tailoring the nanostructures of the alloys and/or supporting them with porous conducting materials [i.e., carbon, NF, and copper foam (CF)]. Hence, the PMMAs for LIB anodes are classified according to the main active atoms/elements in the alloy compositions: (i) tin (Sn)-based alloy anodes; (ii) cobalt (Co)-based alloy anodes; (iii) manganese (Mn)-based alloy anodes; and (iv) other alloy anodes-containing active elements/atoms (i.e., Fe, V, Ni, Zn, Ti, Si).

Porous multimetallic tin (Sn)-based alloy anodes

The high theoretical capacity, cheap nature and suitable working conditions of Sn have positioned it as a capable anode for imminent LIBs. The practical application of Sn anodes is limited by the huge volume change during Li^+-ions lithiation and delithiation, which results in massive irreversible capacity loss and poor life cycle. Alloying of Sn to other metals/composites with carbon having tailored morphologies and augmented synergism is desirable for boosted electrochemical properties of energy storage systems[53,54], particularly improving the anodic performance of porous multimetallic Sn-based alloy anodes in LIBs[55]. For example, the construction of Sn on a porous Cu foam substrate (Sn-Cu_6Sn_5/Cu foam) was achieved by electrodeposition. This configuration exhibited superior performance as a LIB anode at higher initial SC (821.5 mAh/g@0.1 A/g) compared to Sn/Cu foil (655.5 mAh/g); besides, CR = 58% after 50 cycles, due to the formation of porous Cu_6Sn_5 interface that eschewed volume expansion and pulverization/delamination[56]. This study revealed that Cu foam is a preferred substrate to Cu foil. Template-like electrodeposition/annealing was used to form Sn-Sb on a Cu foil (Sn-Sb/Cu) with a sponge-like porous membrane alloy on the Cu foil through a mixed phase inversion process and tested as a LIB anode[57]. In the 1st cycle, Sn-Sb/Cu anode delivered impressive SC (651.9 mAh/g@0.5 A/g), CR (82.9%) and rate performance, attributable to the co-existence of alloy on meshwork conducting polymers, unfilled pores and intermediate Cu_3Sn alloy. Although this method proves promising, more robust research is needed for directing the structures of the PMMAs with improved energy storage capacity and stability.

Sb-doped SnO_2 nanoparticles grown on N-doped graphene-carbon nanotubes hydrogels (ATO/N-GCH) were prepared by a hydrothermal method and then freeze-drying to obtain the aerogel counterpart (ATO/N-GCA) [Figure 6A], with endowed 3D spherical Sb-SnO_2 on sheet-like nanotube proved by scanning electron microscopy (SEM, Figure 6B), high porosity and electrical conductivity to afford good LIB anode performance at increased initial SC (942 mAh/g@1.0 A/g), CR (73%) and rate capability than ATO/G (~940 mAh/g; 59%) and SnO_2/N-GCA (~940 mAh/g; 35%) [Figure 6C-E][58]. Indeed, metal doping and/or composite with metal influences the electrical conductivity of Sn-based anodes for enhanced electrochemical energy storage capability. $CoSn_2$ and $FeSn_2$ tetragonal nanocrystals, proved by the transmission electron microscope (TEM, Figure 6F), were separately prepared by a chemical reduction method[59]. The $CoSn_2$ possessed higher average SC (650 mAh/g@1.984 A/g) and excellent cycling stability, relative to an equivalent mixture of metals (Co + Sn, 380 mAh/g) and Sn (520 mAh/g) [Figure 6G], due to the presence of Co domains that buffered the volumetric change during cycling, eschewed Sn aggregation and amorphization. However, amorphous $CoSn_2O_x$ nanoparticles with spherical morphology, proved by TEM [Figure 6H] prepared by chemical reduction and ball milling in air, displayed better mean SC (525 mAh/g@2.0 A/g) and cycling performance than crystalline $CoSn_2$ (462 mAh/g; 82%) [Figure 6I-K][60]. This was ascribable to the inhibition of Li alloy formation, the buffering effect of inactive Co matrix on the volume change, and the prevention of Sn agglomeration during lithiation/delithiation. The modulated physicochemical merits such as defects and oxygen vacancies of amorphous anodes are beneficial for enhanced energy storage.

Porous multimetallic cobalt (Co)-based alloy anodes

In recent times, Co-based materials (i.e., oxides, phosphides, nitrides, sulfides and alloys) are receiving huge attention as impressive anodes and electrocatalysts for LIBs and other electrochemical applications, owing to their excellent electrochemistry[61]. Despite this, the anode is still affected with volume variations triggered by the lithiation/delithiation that lead to the pulverization and detachment, thereby causing capacity fading[62]. This issue could be circumvented by rational nanoarchitecture design and alloying with or without conductive materials in facilitating the rapid Li^+ ions diffusion and enduring strain induced by the volume enlargement, thereby augmenting the electrochemical activity and cyclability[63,64]. For instance, $NiCo_2O_4$ anchored reduced graphene oxide (rGO/$NiCo_2O_4$) was systematically synthesized by citrate-assisted hydrothermal/annealing techniques, which enabled interconnected nanosheets on hierarchical porous wrinkled film to give high initial SC (1,697.9 mAh/g@0.2 A/g), notable CR and rate capability[65]. The high capacity was traced to contributory effects of the hierarchical porous support that optimized electrode/electrolyte interface for rapid Li^+-ions flux/diffusion. Appropriate hierarchical nanocomposites are excellent materials for outstanding reversible Li^+-ion storage. Hard-template annealing was utilized to construct CuO/CoO core/shell arrays on Cu foams [Figure 7A], which gave very good LIB anode performance at initial SC (1,216 mAh/g@0.1 A/g). Then, this capacity increased to 1,364 mAh/g after 50 cycles, with a CE of 69% [Figure 7B][66], due to the unceasing polymeric gel/oxide layer formation on the nanosized metal oxides. Meanwhile, the high SC and impressive CR (93.8%) after 1,000 cycles [Figure 7C] were ascribed to the unique porous 3D hierarchical tubular core/shell structure, as proved by SEM [Figure 7D], and potent hybridization. The fabrication of hollow heterostructures is amongst the most practicable strategies for high-performance energy storage systems.

Various self-supported hierarchical porous multimetallic oxides ($ZnCo_2O_4$, $NiCo_2O_4$, $Cu_xCo_{3-x}O_4$, $Mn_xCo_{3-x}O_4$, $Zn_xNi_yCo_{3-x-y}O_4$, Co_3O_4, NiO, Fe_2O_3 and ZnO) on Ni foam (NF) were developed by hard-template/calcination[67]. The $ZnCo_2O_4$/NF had improved interfacial Li^+-ion storage, numerous interconnected flower-like nanosheets and reversible polymeric gel-film formation/dissolution to deliver a higher LIB anode at initial SC (1,544 mAh/g@0.1 A/g), CR (82%) and cycling performance, than

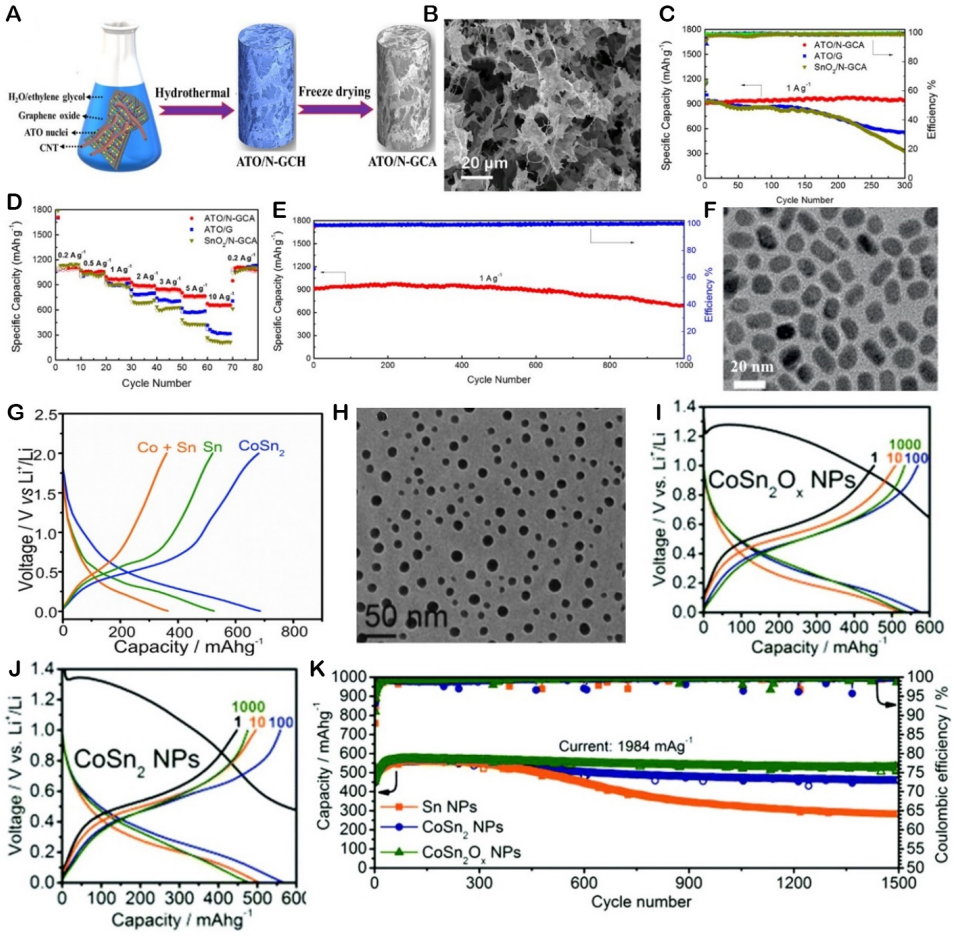

Figure 6. (A) Hydrothermal synthesis, (B) SEM, (C) rate capability and (D and E) cyclic performance of ATO/N-GCA, ATO/G and SnO_2/N-GCA. This figure is quoted with permission from Ref.[58] Copyright 2017 Elsevier. (F) TEM and (G) galvanostatic charge/discharge curves of $CoSn_2$, Co + Sn and Sn. (H) TEM, (I and J) galvanostatic charge/discharge and (K) cycling stability of $CoSn_2O_x$, $CoSn_2$ and Sn NPs. This figure is quoted with permission from Refs.[59,60] Copyright 2018 the Royal Society of Chemistry.

$NiCo_2O_4$/NF (1,500 mAh/g; 70%); $Mn_xCo_{3-x}O_4$/NF (1,300 mAh/g; 73%), Co_3O_4/NF (1,280 mAh/g; 70%) and NiO/NF (1,250 mAh/g; 65.6%). Mesoporous multimetallic alloy oxides are promising anodes with high yields for outstanding Li^+-ion storage capacity. Porous $NiCo_2O_4$/NiO hollow dodecahedron (HD), proved by FESEM [Figure 7E], was prepared from a zeolitic imidazolate framework-67 (ZIF-67) sacrificial template via solvothermal/calcination[32]. The $NiCo_2O_4$/NiO-HD demonstrated high SC (1,622 mAh/g@0.2 A/g) at the 1st cycle, incredible CR (97.2%) and cycling performance [Figure 7F and G], compared to Co_3O_4-HD, owing to its unique hierarchical nanostructures, high surface area, acceptable volume increase, high electron mobility and rapid Li^+-ions diffusion. However, chemical reduction synthesis of $NiCo_2O_4$, utilizing PVP as a structure-directing agent, gave lower initial SC (1,282 mAh/g@1.0 A/g), but moderate irreversible capacity fading (6%) [Figure 7H], which was traced to its endowed porous rose flower-like nanosheets, as proved by FESEM [Figure 7I], which provided enough void space for easy electrolyte penetration and rapid electron mobility[68]. These studies proved the superiority of metal-organic framework (MOF)-templated anodes for excellent Li^+-ion storage performance, owing to the tailored nanoarchitectures and porosity.

Mesoporous $FeCo_2O_4$ was synthesized via sol-gel/calcination, which favorably utilized its multicomponent effect, octahedral architectural stability and meso-porosity for superb LIB anode performance at increased

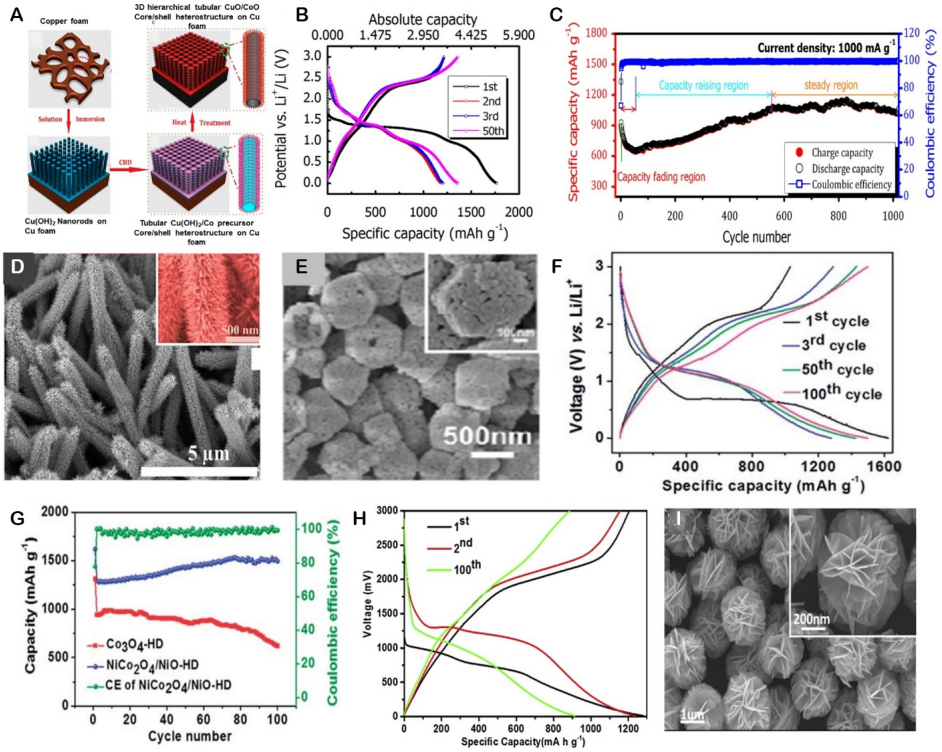

Figure 7. (A) Hard-template fabrication method, (B) charge/discharge curves, (C) cyclic performance at 0.1 A/g and (D) SEM of tubular CuO/CoO core/shell arrays on Cu foam. This figure is quoted with permission from Ref.[66] Copyright 2015 Elsevier. (E) Field emission scanning electron microscopy (FESEM), (F) charge/discharge curves for 1st, 3rd, 50th and 100th cycles, and (G) cycling performance of $NiCo_2O_4$/NiO-HD at 0.2 A/g. This figure is quoted with permission from Ref.[32] Copyright 2015 the Royal Society of Chemistry. (H) charge/discharge curves of 1st, 2nd and 100th cycles at 1.0 A/g, and (I) FESEM of $NiCo_2O_4$. Reproduced with permission from Ref.[68] Copyright 2016 Elsevier.

initial SC (2,436 mAh/g@0.2 A/g) and CR (95.2%)[69]. The 3D Zn-Ni-Co oxide enclosed graphene nanosheets (ZNCO/GNS) were prepared by chemical reduction/hard-template annealing [Figure 8A][70]. This was based on the wrapping of ZNCO microspheres within the GNS to form core/shell architectures, evidenced by SEM [Figure 8B], that prevented agglomeration of active ZNCO, volume variations, and boosted electrons/Li^+-ions mobility, which resulted in good Li^+-ion storage at initial SC (1,429 mAh/g@0.1 A/g) and CR (95%) [Figure 8C]. Adopting synthesis method for preparing core/shell composites with micro-/nanostructures are preference for boosted Li^+-ion storage. The fabrication of 3D porous $ZnCo_2O_4$ thin films on NF ($ZnCo_2O_4$ thin film/NF) via hard-template annealing gave high discharge capacity (1,726 mAh/g@0.4 A/g) and cycling performance[71]. This was due to the capability of the 3D porous $ZnCo_2O_4$ architectures in facilitating abundant reactive sites, effective void space to volume change during cycling, increased contact with electrolyte and boosted electron mobility. Core/shell Te@ZIF-8 (Zn,Co) nanofibers were prepared by hydrothermal methods and explored as sacrificial templates via annealing to afford 1D hierarchical Te@$ZnCo_2O_4$ nanofibers, proved by TEM [Figure 8D] with fascinating compositional and morphological merits to deliver great LIB anodes at high SC (1,364 mAh/g@0.1 A/g), eminent cycling durability (~100%) and rate capability [Figure 8E and F][72]. Also, the fabrication of Zn-Co-S embedded N,S-codoped carbon polyhedral (Zn-Co-S@NS-CP), prepared from the annealing of ZIF-8@ZIF-67 template, was endowed with hierarchical hollow polyhedron architectures with interconnected conductive network, more reactive active sites, Li^+-ion mobility and phase separation of lithiated intermediates that enabled LIB anodes with high reversible capacity at SC (1,298.1 mAh/g@0.57 A/g) and long-term stability[73]. The SC could be affected by changing the annealing

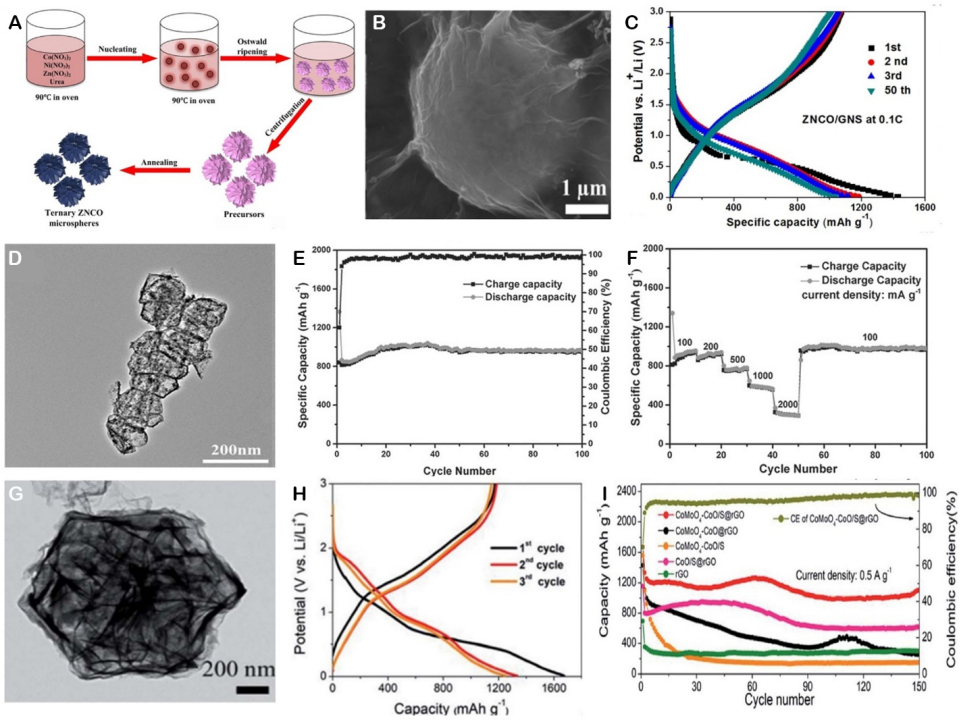

Figure 8. (A) Chemical reduction/annealing synthesis, (B) SEM, and (C) charge/discharge curves at 0.1 A/g for 1st-3rd and 50th cycles of ZNCO/GNS. (D) TEM, (E) Charge-discharge, cycling life and Columbic efficiency, and (F) rate capability of Te@$ZnCo_2O_4$ nanofibers. This figure is quoted with permission from Refs.[70,72] Copyright 2015 Wiley-VCH. (G) TEM, (H) 1st-3rd charge/discharge profiles and (I) Cyclic performance at 0.5 A/g of $CoMoO_4$-CoO/S@rGO and analogs. This figure is quoted with permission from Ref.[75] Copyright 2022 the Royal Society of Chemistry.

temperature during the anode preparation. Thereby, lower SC (975.2 mAh/g@0.2 A/g) and CR (81.6%) were recorded for spherical CoO-ZnO@NC-450, prepared by hydrothermal/calcination of CoZnBTC@NC precursors at various temperatures (350-550 °C in Ar for 2 h), owing to the disordered structure at 450 °C that reduced the permeation energy barrier and abundant active sites of Li^+-ions[74].

Hierarchical porous $CoMoO_4$-CoO/S@rGO, prepared from MOF-template via S-doped hydrothermal/annealing method, had core/shell polyhedron structures, proved by TEM [Figure 8G] to deliver better LIB anode at increased initial SC (1,672 mAh/g@0.5 A/g), and excellent cyclic performance superior to $CoMoO_4$-CoO@rGO, $CoMoO_4$-CoO/S, CoS/S@rGO and rGO [Figure 8H and I][75]. This study revealed that S-doping enlarged the interplanar distance, improved conductivity and charge storage capacity, which were beneficial for high-performance LIB anodes. The fabrication of a porous Cu shell uniformly glazed on CoO nanowires core (CoO/Cu) was achieved by hard-template/pulsed electrodeposition[76]. The constructed CoO/Cu heterostructured arrays exhibited impressive performance as anodes in LIBs at higher initial SC (1,215 mAh/g@0.5 A/g) and CR (68.15%) than CoO (1,053 mAh/g; 53.8%), due to their improved electron/ion transport, conductivity, surface area, and lower polarization.

Porous multimetallic manganese (Mn)-based alloy anodes

Manganese oxide (Mn_xO_y)-based materials possess inimitable outer valence electrons, physical and chemical features that makes it amazing LIB anodes[77,78]. Besides their low cost, environmental benignity, ease of preparation and high theoretical capacity (1,232 mAh/g). Nevertheless, large volume change during cycling and low electrical conductivity of Mn_xO_y anodes are the drawbacks that lead to low rate capability and

cycling durability[79,80]. These drawbacks are solved by deliberately fabricating porous nanostructured Mn_xO_y alloy and/or carbon composites with controlled sizes and morphologies[81-83]. For instance, solvothermal/annealing methods were utilized to fabricate porous quasi-mesocrystal $ZnMn_2O_4$, following oriented attachment and Ostwald ripening mechanisms for the formation of distinct twin-microsphere structures, 3D hierarchical porosity and Li alloying reaction, beneficially utilized for good LIB anodes at initial SC (1,100 mAh/g@0.5 A/g), CR (77.8%), rate capability and long-standing cycling durability[84]. However, porous $ZnMnO_3$ spherulite, prepared by co-precipitation/annealing, had inner atomic synergism of Zn-O and Mn-O that decreased its LIB anode performance at lower initial SC (1,294 mAh/g@0.5 A/g), but improved CR (67.9%) than ZnO-MnO_2 equimolar power mixture (1,333 mAh/g; 60.4%) and nano-sized MnO_2 (1,553 mAh/g)[85]. This study showed that the synergistic effect of inner atoms of Zn-O and MnO_2 could lead to significant initial capacity fading of $ZnMnO_3$, but improved rate capability and cyclability. The construction of 3D porous $CoMn_2O_4$ on NF ($CoMn_2O_4$/NF) was achieved by hard-template/annealing, with greater initial discharge SC (1,833 mAh/g@0.4 A/g) and CR (74.5%), compared to un-annealed $CoMn_2O_4$/NF (1,540 mAh/g, 60.6%)[86]. Thus, annealing enabled high synergism in $CoMn_2O_4$/NF for improved initial SC via enhanced reaction sites, electrode-electrolyte contact and electron mobility, nullified volume change and improved growth/dissolution of polymeric gel film attachment on the $CoMn_2O_4$ anode. However, annealing had suppressing effect on $ZnMn_2O_4$/NF, thereby un-annealed $ZnMn_2O_4$/NF displayed better initial discharge SC (2,211 mAh/g@0.4 A/g), but lower CR (94%) than annealed $ZnMn_2O_4$/NF (1,789 mAh/g; 96%)[87]. The studies confirmed that effects of annealing are ambiguous for boosting the SC of Mn_2O_4-based anode/NF anodes but definitely augments their CR and cycling stability.

Controlled synthesis of multi-shelled nanostructured Ni-Co-Mn oxides by self-templated hydrothermal/annealing method [Figure 9A] that enabled various architectures, including quadruple-shelled hollow microspheres (QS-HS), triple-shelled hollow microspheres (TS-HS) and double-shell hollow microspheres (DS-HS), proved by TEM [Figure 9B-D][88]. The QS-HS afforded abundant interfacial electrode-electrolyte interaction, numerous active sites, and favorable Li^+-ions transfer and volume accommodation to deliver high LIB anodes at initial SC (1,761.8 mAh/g@0.2 A/g), rate capability (1,073.6 mAh/g@5 A/g), gravimetric energy densities (1,261.7 Wh/kg) and good cyclability, compared with TS-HS and DS-HS [Figure 9E-G]. Rational design of multi-shelled PMMA oxides with tailored morphology and compositions is an appropriate recipe for the practicality of LIB anodes. A double-shelled NiO nanoparticles-doped MnO grown on NF (np-Ni@NiO/MnO/NF), prepared by an induction melting/dealloying/annealing, gave impressive initial reversible SC (960 mAh/g@0.1 A/g), remarkable CR (105%), CE and rate capacity [Figure 9H and I], due to its interconnected shell nanoporous architectures with vigorous defects and roughness, evidenced by SEM [Figure 9J], that allowed high ions/electrons mobility and shielded volume expansion[89]. Dealloying and oxidation of PMMAs allow a sporadic distribution of core-shell nanocrystals on conductive support for excellent LIB anodes. Solvothermal/annealing strategy was used to prepare porous $Zn_{1.67}Mn_{1.33}O_4$ microspheres anchored GNS ($Zn_{1.67}Mn_{1.33}O_4$/GNS), where the GNS eschewed aggregation of the cubic spinel-type oxide, enhanced its electrical conductivity and alleviated volume change to deliver superior cyclability, (99.95%), retentive capacity (670 mAh/g@0.1 A/g) after 200 cycles, lower than $Zn_{1.67}Mn_{1.33}O_4$ (99.81%; 518 mA/g)[90]. The fabrication of well-dispersed spinel-oxides incorporated GNS is effective for buffering the volume variations.

A series of NiMn hydroxides modified with [p-phthalic acid (PTA)] and/or activated carbon (AC) [i.e., $Ni(OH)_2$/$Mn(OH)_2$ (MN-1), NiO/Mn_3O_4 (MN-2), MN-1/P, $Ni(OH)_2$/$Mn(OH)_2$/AC) (MN-1/C), $Ni(OH)_2$/$Mn(OH)_2$/PTA/AC (MN-1/PC), NiO/Mn_3O_4/PTA (MN-2/P), NiO/Mn_3O_4/AC (MN-2/C), and NiO/Mn_3O_4/PTA/AC (MN-2/PC)] were synthesized by *in-situ* electro-conversion/calcination and studied as LIB anodes[91]. The MN-1/P showed higher initial discharge SC (1,554 mAh/g) than MN-1/PC (1,518 mAh/g),

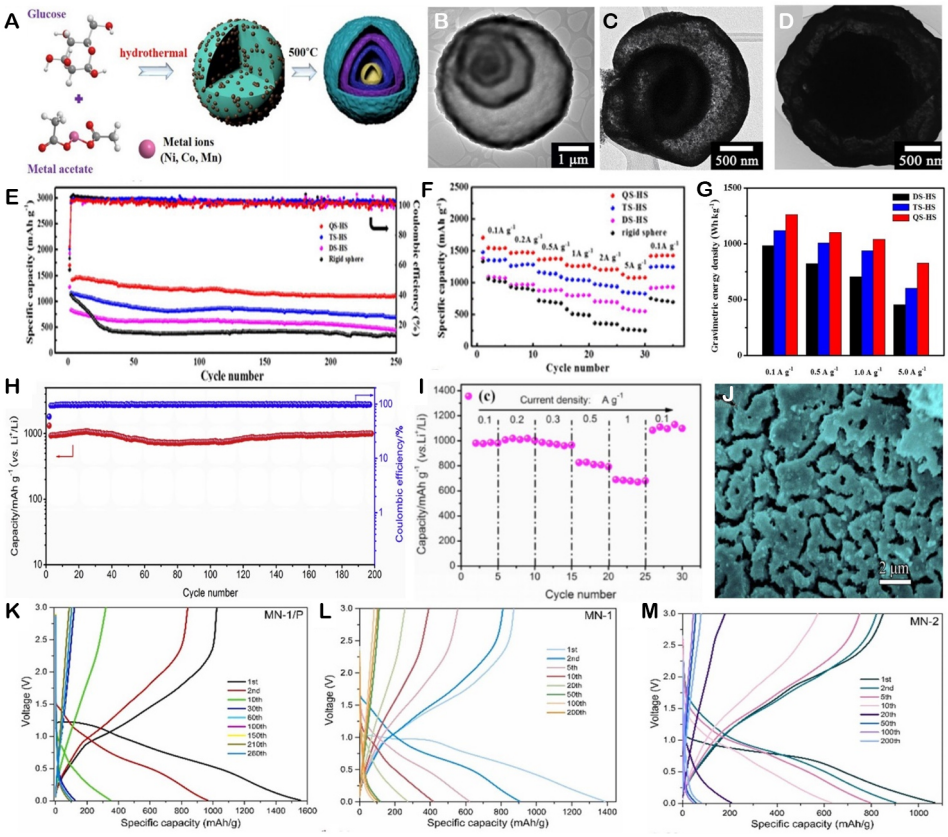

Figure 9. (A) Controlled hydrothermal/annealing synthesis, (B-D) TEM, (E) specific capacity and coulombic efficiency, (F) rate performance, and (G) gravimetric energy densities of Ni-Co-Mn oxides QS-HS, TS-HS and DS-HS. This figure is quoted with permission from Ref.[88] Copyright 2017 the American Chemical Society. (H) capacity retention at 0.1 A/g after 200 cycles and coulombic efficiency, (I) rate capacity at various current densities, and (J) SEM of np-Ni@NiO/MnO/NF. (K-M) charge/discharge profiles of MN-1/P, MN-1, and MN-2. This figure is quoted with permission from Refs.[89,91] Copyright 2019, 2023 Elsevier.

MN-1 (1,386 mAh/g), Mn-2/P (1,128 mAh/g) and MN-2 (1,068 mAh/g) [Figure 9K-M], besides its CR (100%), owing to the successful wrapping of NiMn nanosheets by the PTA, dissolved by alkaline medium ($^{-}$OH), without changing the MN-1 structure and content (1:1). The facile *in-situ* electrosynthesis of NiMn-MOF for the development of LIB anodes is viable for large-scale application of LIBs. Microsphere 3D Cu/Mn_3O_4@SC composite, made from thermolysis of Cu-Mn/MOF template, had an impressive anodic performance for Li^+-ion storage at good SC (766.2 mAh/g@0.2 A/g), and CR (66.3%), attributable to the heterojunction synergism[92]. The synergetic effect of the components of multimetallic alloy anodes is significant for their increasing conductivity and Li^+-ion diffusion rate.

Other porous multimetallic-based alloy anodes

Other PMMAs with main active atoms/elements, including Fe, Mo, Ni, Si, Ti, V, and Zn, and their composites have been demonstrated as inspiring anodes for LIBs because of their excellent features (i.e., chemical stability, high ionic/electrical conductivity and lithiophilicity) that facilitate facile Li^+-ions mobility and inhibit Li dendrite growth and volume expansion[93-95]. For example, the fabrication of TiO_2 on Fe_3O_4/CNTs (TFCs) was achieved by hydrothermal/calcination [Figure 10A], based on the bottom-up assembly mechanism with TiO_2, carbon nanotubes (CNTs) and Fe_xO_y as buffer material, conducting network/effective anchorage and active nanoteeth, respectively, proved by HRTEM [Figure 10B][96]. The TFCs exhibited higher initial SC (1,589 mAh/g@0.5 A/g) than Fe_xO_y/CNTs (FCs, 771 mAh/g) and CNTs

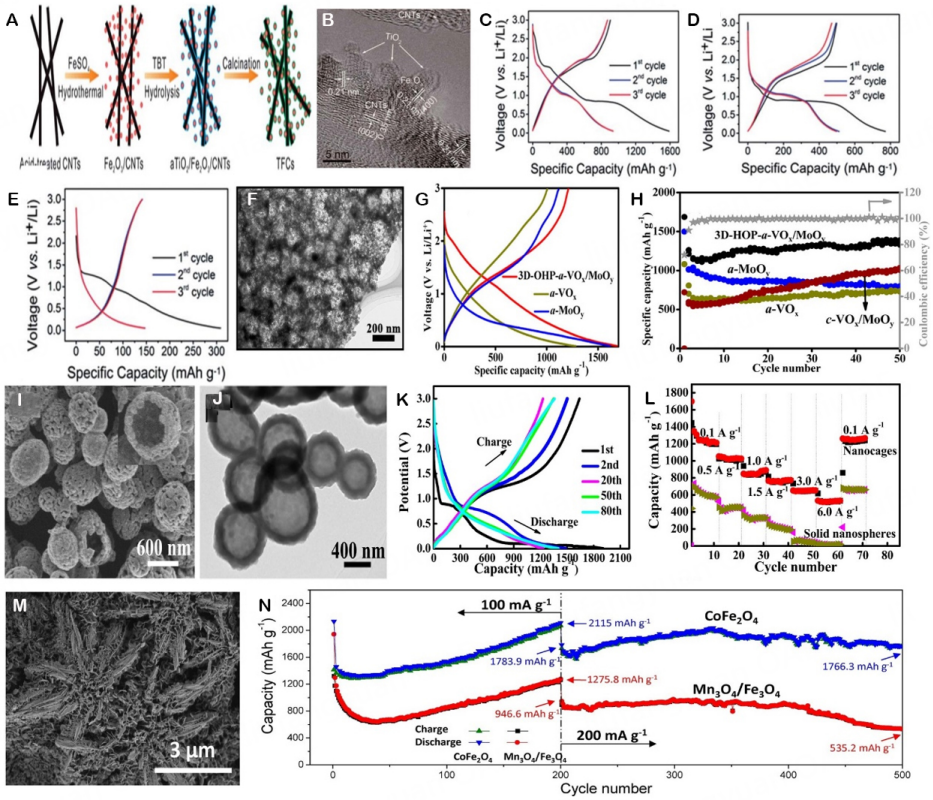

Figure 10. (A) Hydrothermal/calcination, (B) HRTEM and (C-E) galvanostatic charge/discharge curves of TFCs, FCs and CNTs at 0.05 A/g. This figure is quoted with permission from Ref.[96] Copyright 2014 the Royal Society of Chemistry. (F) TEM, (G) charge/discharge curves at 0.2 A/g and 1st cycle, and (H) cycling performance and CE of 3D-OHP-a-VO_x/MoO_y, VO_x/MoO_y, a-VO_x, and a-MoO_y. Adapted with permission from Ref.[97] Copyright 2016 the American Chemical Society. (I and J) SEM, (K) charge/discharge profiles, and (L) rate performance of $Zn_3V_2O_8$ hollow nanocages and solid nanospheres. (M) SEM and (N) cycling performance of $CoFe_2O_4$ and Mn_3O_4/Fe_2O_4. This figure is quoted with permission from Ref.[98,99] Copyright 2017 Elsevier.

(309 mAh/g) [Figure 10C-E], and its superb rate capability and cycling performance, due to its highly porous hierarchical structural integrity. The scalable synthesis of hybrid anodes with specific morphologies/architectures and compositions is crucial in high-performance LIBs.

The 3D ordered hierarchical porous amorphous vanadium and molybdenum oxides (3D-OHP-a-VO_x/MoO_y), prepared by freeze-drying/annealing, showed remarkable Li^+-ion storage[97]. The 3D-OHP-a-VO_x/MoO_y exhibited amorphous architectures and 3D hierarchical sheets, proved by TEM [Figure 10F], and strong synergism that facilitated enhanced initial discharge SC (1,705 mAh/g@0.1 A/g) relative to crystalline VO_x/MoO_y (721 mAh/g), a-VO_x (1,600 mAh/g), and a-MoO_y (1,270 mAh/g), besides good cycling durability (82.1%) and rate capability [Figure 10G and H]. This study established the significant benefits of amorphous nanostructures with well-defined structures and compositions for high-performance anodes in LIBs. Solvothermal/annealing methods were exploited to develop porous $Zn_3V_2O_8$ hollow nanocages and solid nanospheres, evidenced by SEM [Figure 10I and J] and comparatively tested as LIB anodes[98]. The hollow nanocages displayed superior Li^+-ion storage at higher initial discharge SC (1,906 mAh/g@0.1 A/g) [Figure 10K], which was 1.5-folds of solid nanospheres (1,285 mAh/g), good rate capability [Figure 10L] and CR (80%). This was ascribable to the rapid Li^+-ions/electrons diffusion, facile electrolyte permeability and optimal volume change alleviation by the hollow nanocages. Hence, hollow cages are preferred architectures to solid nanospheres for excellent LIB anodes. $CoFe_2O_4$ and Mn_3O_4/Fe_2O_4

were fabricated by melt spinning/dealloying, where $CoFe_2O_4$ with interconnected nanoplates/sheet-like architectures and porosity, evidenced by SEM [Figure 10M], high contact surface for Li^+-ion mobility, rapid diffusion and smaller size that gave outstanding LIB anodes at higher initial discharge SC (2,134.7 mAh/g@0.1 A/g) and CR (83.5%), relative to Mn_3O_4/Fe_2O_4 (1,942.9 mAh/g; 66.9%) [Figure 10N][99]. Well-constructed PMMA composition and dealloying is a possible approach for large production of LIB anodes with amazing performance.

Inverse spinel-type $NiFe_2O_4$ anchored porous carbon fibers (NFO@C), synthesized by electrospinning/calcination, delivered superior LIB anodes to NFO, which was attributable to exclusive mesoporous fibrous structures, high surface area, fast Li^+-ions diffusion, and improved electrical conductivity that eventually eschewed pulverization and agglomeration[100]. The physicochemical merits of mesoporous fibrous supports could significantly boost the electrochemical storage capacity of PMMA oxides. Facile evaporation-solidification/annealing was adopted to prepare vacancy-enriched $Ni_3ZnC_{0.7}$ nanohybrids, with much focus on stoichiometric and non-stoichiometric ratios, where the latter gave higher Li^+-ion storage capacity (1,100 mAh/g@0.05 A/g), rate capability and cycling stability than the former (400 mAh/g)[101]. This study proved that a non-stoichiometric ratio of PPMA alloy carbides induces vacancies/defects that increased capacitive and diffusion-controlled charge-storage features, and Li^+-ions adsorption, relative to the stoichiometric counterparts. A series of porous transition metal-Si-carbon composites (i.e., $NiSi_x$/Si/C, $CoSi_x$/Si/C, and $TiSi_x$/Si/C) were fabricated by ball-milling/annealing. Among the composites, $NiSi_x$/Si/C had higher initial SC (1,060 mAh/g@0.1 A/g), rate capability and CR than $CoSi_x$/Si/C (930 mAh/g) and $TiSi_x$/Si/C (832 mAh/g), due to its porosity and high specific area[102]. However, NiFe-$NiFe_2O_4$/rGO composites with adjustable mass ratios, synthesized by chemical reduction/calcination at various time (2-10 h)[103]. The optimized NiFe-$NiFe_2O_4$/rGO-8 anode at calcination time (8 h) gave impressive initial discharge SC (1,362 mAh/g@0.1 A/g) and CR (79.4%), amongst others, owing to its distinct composition, hollow microstructure, and optimal synergism. Optimizing the preparation conditions of binary MA oxide composites is necessary to tune the Li^+-ion storage. The 3D porous ternary Ni-Co-Fe oxides ($NiO/Co_3O_4/Fe_3O_4$) hollow nanostructures were made by solution-precipitation/calcination and tested as a LIB anode[104]. The $NiO/Co_3O_4/Fe_3O_4$ exhibited superior initial discharge SC (1,052 mAh/g@0.5 A/g), CR (92.4%) and CE, compared to Co_3O_4/Fe_3O_4 (~920 mAh/g; 85.7%), ascribable to the improved synergistic effect of Ni-Co-Fe ternary hollow nanocage architectures that boosted the transportation efficiency, amplified interfacial capacitance, and decreased contact barrier. Synergism of ternary PMMA oxides significantly changes the physicochemical merits advantageously used for improving the Li^+-ion storage, relative to binary counterparts. MOF templates were utilized for the construction of 3D $NiCo_2O_4@Fe_2O_3$, with flower-like cross channel and surface crumpled structures, which delivered more reliable LIB anodes at high initial discharge SC (1,640 mAh/g@1.0 A/g) that was three folds of $NiCo_2O_4$ (1,261.5 mAh/g; 52.9%)[105]. However, $CoNiSe_2$/C-700 fabricated from MOF templates exhibited outstanding Li^+-ion storage at superior initial discharge SC (2,125.5 mAh/g@0.1 A/g), CE (98%) and long-term cycling performance, due to the synergism of the binary metal selenides, well-defined nanododecahedral architectures, improved electronic structure and fast charge transport at the electrolyte interface[106]. The enhanced LIB anode of the $NiCo_2O_4@Fe_2O_3$ was related to better conductivity, lower electrode interfacial barrier, porous channel structure and synergy between Ni-Co petal-like and crumpled Fe_2O_3 coating.

Sodium-ion batteries

The abundance and low cost of sodium (Na) have spurred the Sodium-ion batteries (SIBs) among the most auspicious energy storage technology[107,108]. The practicability of the SIBs lies largely on robust fabrication of electrodes with high SC and long cyclability. The development of suitable anodes is more thought-provoking; in this regard, the PMMA anodes have great potential for SIBs with high energy because of their high gravimetric/volumetric SCs and easy Na^+-ion insertion/ejection[109-111]. The utilization of PMMA anodes

for viable SIBs is conspired with enormous capacity fading, irreversible capacity, rate capability, low coulombic efficiency and poor cycling durability that lead to volume expansion[112,113]. This hitch is solved by incorporating conductive materials with their unique physicochemical merits that could accelerate the reaction kinetics and alleviate capacity fading[114-116]. Hence, the modulated physicochemical features of the PMMA anodes result in improved Na^+-ion storage and stability. For example, a hydrothermal method was exploited to prepare Sb-doped SnO_2 nanoparticles grown on N-doped graphene-carbon nanotubes aerogels (ATO/N-GCA) with spherical Sb-SnO_2 on sheet-like nanotubes, high porosity and electrical conductivity that delivered increased initial SC (409 mAh/g@0.1 C), CR (74%) and lower charge transfer resistance (R_{ct} = 314 Ω) than ATO/G (124 mAh/g; 59%, 475.6 Ω)[58]. This was traced to the rapid Na^+-ions diffusion, instead of electrons, on SnO_2 and macroporosity for easy contact and sodiation/desodiation during cycling. However, ultra-small SnSb nanocrystals embedded N-rich porous carbon nanowires (SnSb/N-PCNWs), synthesized by electrospinning/calcination [Figure 11A], were endowed with enhanced electronic properties, plentiful edges/defects for rapid Na^+-ions adsorption, robust spherical metals on nanowires, proved by SEM and TEM [Figure 11B and C], crystalline-phase reservation and highly reversible alloying/dealloying behavior that facilitated its boosted SIB anode at superior rate capability, CR (100%) and cycling performance, compared to counterpart without urea (SnSb/CNWs), PCNWs and bulk SnSb [Figure 11D and E][117]. Distinctive nanoarchitectural design of PMMA anodes with alloying/dealloying nature allows an extremely long lifespan for SIBs.

The construction of bimetallic metals core-shells ($SnSe_2$/$CoSe_2$@C), achieved by selenization/carbonization and tested as SIB anodes, showed higher initial SC (455 mAh/g@0.1 A/g), rate capability and CR (77.6%) than $SnSe_2$/$CoSe_2$ (300.31 mAh/g) and mechanically-mixed $SnSe_2$-$CoSe_2$ (29 mAh/g)[118]. This study proved that the addition of carbon to $SnSe_2$/$CoSe_2$ improved the conductivity, retained the architectural design, and prevented capacity fading. Also, poor chemical bonding in multiple metal selenides results in capacity fading and structural damage. A self-adaptive Sn-Bi@C composite, prepared by hydrothermal/annealing, had Bi-core with Sn shell that exhibited uniform stress circulation, alleviated structural strain, improved electrical conductivity and Na^+-ions diffusion kinetics, advantageous to deliver high SC (462 mAh/g@0.1 A/g) superior to Bi@C (232 mAh/g), Sn@C (374 mAh/g) and pure Sn (219 mAh/g), besides its outstanding CR (86.9%) and cycling performance[119]. This study proved the merits of biphase mixing of metal atoms in PMMA anodes for efficient Na^+-ion storage.

Porous carbon-supported Zn-Mn selenides (ZMS@FC) were constructed by solvothermal/calcination, and examined as SIB anodes[120]. The ZMS@FC was endowed with flower-like metal selenides on flakes support, proved by SEM [Figure 11F] that enabled outstanding initial SC (494.8 mAh/g@0.2 A/g), great rate capability, and CR (74.7%) [Figure 11G-I], compared to MnSe@C (230.9 mAh/g) and ZnSe@C (343.2 mAh/g). This was ascribed to the synergism of the flower-like binary selenides and porous carbon flakes. This study revealed that multimetallic chalcogenides are promising anodes for Na^+-ion storage and stability.

Also, ultrathin $Cu_4Mo_6Se_8$ grown on carbon skeleton (CMSe/C), achieved by chelation/annealing and tested as SIB anode, exhibited exceptional rate capability, initial discharge SC (514 mAh/g@0.5 A/g) and CR (107.7%), relative to $MoSe_2$ (203 mAh/g), ascribable to its copious void space, homogeneous morphology, ultrathin nanosheet arrays and improved conductivity[121]. Moreover, a series of rod-shaped $CoSb_2Se_4$@Sb_2Se_3, i.e., 1CSS, 2CSS and 4CSS at varied Co amounts (0.1, 0.2 and 0.4 mmol), synthesized by hydrothermal, where the optimized Co amount coating in 2CSS anodes of SIB suppressed volume expansion, enhanced structural integrity and cycling stability, and resulted in high CR (81.4%)[122]. This work confirmed the benefits of multimetallic chalcogenide alloy anodes with suitable/appropriate metal atoms

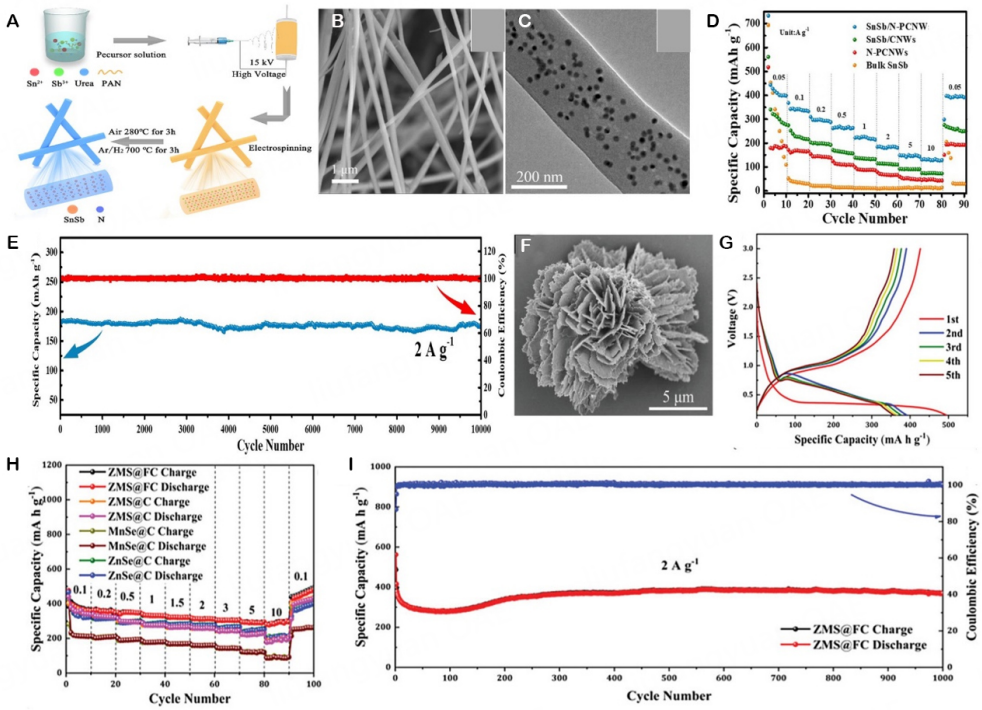

Figure 11. (A) Electrospinning/annealing synthesis, (B) SEM, (C) TEM, (D) rate performance, and (E) ultra-long cyclability of SnSb/N-PCNWs. This figure is quoted with permission from Ref.[117] Copyright 2019 Elsevier. (F) SEM, (G) charge/discharge curves at 0.2 A/g for 1st-5th cycles, (H) rate capability, and (I) long-term cyclability and coulombic efficiency of ZMS@FCs. This figure is quoted with permission from Ref.[120] Copyright 2022 Wiley-VCH.

coating for excellent Na^+-ions diffusion and storage. Chemical reduction/calcination was utilized to construct $NiCoSe_2$ on N,Se codoped carbon ($NiCoSe_2$@NSC) and demonstrated as superior SIB anode at higher SC (572.5 mAh/g@0.2 A/g) and CR (85.1%), relative to $CoSe_2$/NSC (252.7 mAh/g; 82.1%)[123]. This was traced to the synergism, electronic effects, and ions transport of multimetallic selenide alloys, following the probed reaction mechanism by *in-situ* X-ray diffraction (XRD) and theoretical calculations [Figure 12A-E].

VS_4/SnS_2 confined MXene (VS_4/SnS_2@MXene), prepared by hydrothermal/etching/self-assembly, was demonstrated as an anode for Na^+-ion storage, proven experimentally and theoretically[124]. The VS_4/SnS_2@MXene exhibited outstanding SC (2,508.4 mAh/g@0.1 A/g), CR (82.8%) and rate capability, compared to VS_4@MXene and SnS_2@MXene, owing to the heterogenous interfacial interaction that facilitated rapid Na^+-ions, electron mobility, and reduced volume expansion, evidence by the theoretical calculations [Figure 12F-H]. This work proved that construction of heterostructures on conducting 2D network augments the physicochemical merits for high-performance RAMIBs. The influence of partial Mn ion replacement, at various contents (5%-15%), in NiCoS nanosheets, i.e., NCMS-5, NCMS-10 and NCMS-15, was investigated as SIB anodes[125]. This revealed that the NCMS-10 was the optimized ratio with unique structures and more accessible active sites to mitigate the volume expansion and enhance stability, thereby enabling high SC (662.6 mAh/g@0.3 A/g), CR (85.4%), rate capability and long-term cycling stability, amongst others. The appropriate addition of metal atoms in PMMAs is beneficial for excellent Na^+-ion storage. Indeed, the PMMAs are excellent SIB anodes, but only a few studies were reported. There is a need for further exploration of PMMA anodes for SIBs with outstanding performance, cyclability and rate capability.

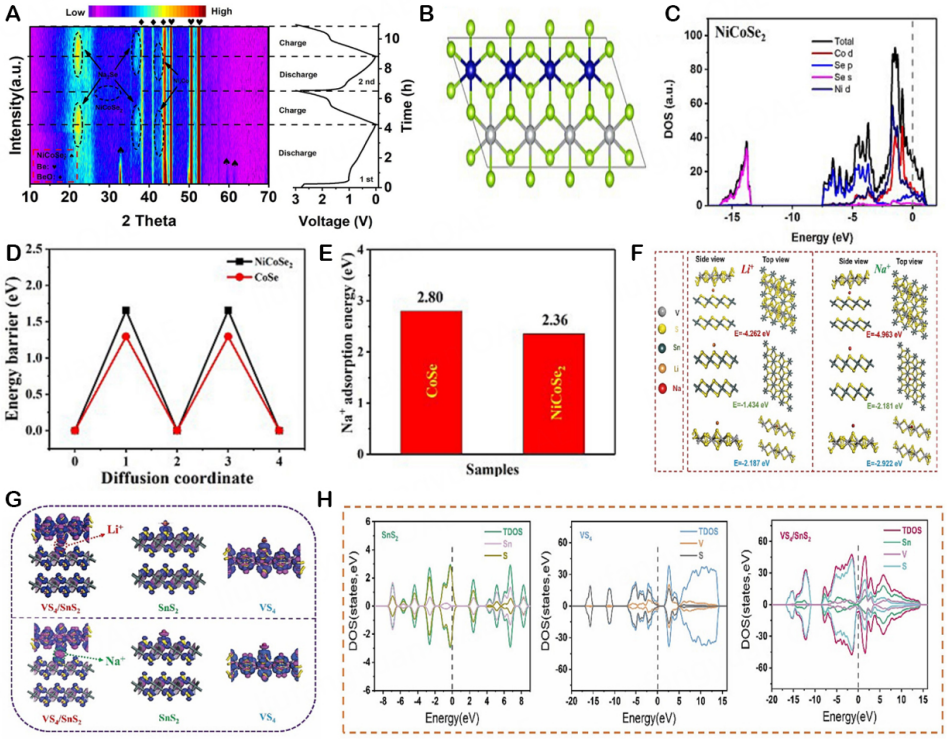

Figure 12. (A) *In-situ* XRD during 1st and 2nd charge-discharge cycles, (B) atomic structure model, (C) density of states, (D) Na^+ ions adsorption energies, and (E) diffusion energy barriers of Na^+ ions of $NiCoSe_2$ and CoSe. (F) Top/side view of most stable adsorption sites, (G) charge density differences of each structure and (H) simulated density of states of VS_4/SnS_2/MXene, VS_4/MXene and SnS_2 /MXene. This figure is adapted from Ref.[123,124] Copyright permission 2024 Elsevier.

Potassium-ion batteries

The Potassium-ion batteries (PIBs) are recently drawing so much interest as an alternative to LIBs and SIBs because of their chemical and economic merits[126]. Their chemical quality is traced to low potential of K^+/K (-2.88 V *vs.* SHE) in carbonate ester electrolytes[127], which infers a high ED with K^+-ions as the charge carrier and a low risk of potassium (K) plating[128]. Also, K^+-ions boost the ionic conductivity and rapid diffusion rate. The economic advantage is due to the essentially limitless and worldwide distribution of K reserve at low cost [i.e., potassium carbonate (K_2CO_3, $1,281/tonne) compared to lithium carbonate (Li_2CO_3, $6,500)][129]. Also, PIBs allow the use of extremely cheap electrode materials and facilitate an easy transition to commercialization with the existing LIB industry. Amongst the commonly used PIB anodes, PMMA anodes are promising with higher capacity and/or power than carbon-based anodes[130]. However, only a few studies reported the performance of PMMA anodes for PIBs. For example, a 3D nanoporous CuBi (NPCuBi) anode was fabricated via melt-spinning/dealloying [Figure 13A], which enabled interconnection of Bi as an active phase and Cu ornamented as a highly conductive matrix with bicontinuous ligament-channel architecture, proved by SEM [Figure 13B], abundant porosity, synergistic effect, and conductivity of CuBi that surmounted slow K^+-ion diffusion kinetics and volume expansion during cycling, and resulted in superior PIB anodes at initial discharge SC (1,045 mAh/g@0.05 A/g), CR (> 93.0%) and rate capability to nanoporous Bi (~650 mAh/g) [Figure 13C and D][131]. Dealloying of Bi-based alloys is an effective strategy for boosting K^+-ion storage and stability.

Flower-like porous carbon-embedded Zn-Mn selenides (ZMS@FC), made via solvothermal/calcination, demonstrated exceptional performance as PIB anodes. They exhibited a great initial SC

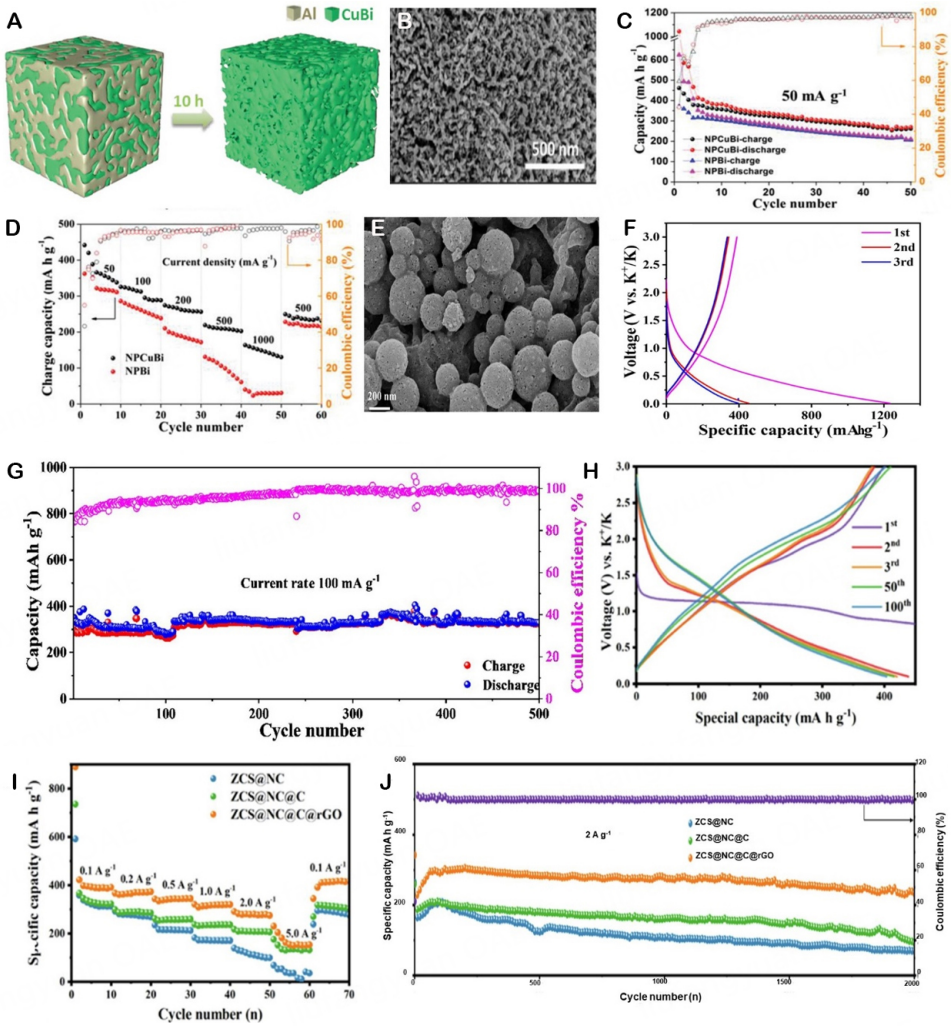

Figure 13. (A) Melt-spinning/chemical dealloying synthesis, (B) SEM, (C) cycling and (D) rate performance for 50 cycles of NPCuBi and NPBi. This figure is quoted with permission from Refs.[131] Copyright 2020 Wiley-VCH. (E) SEM, (F) 1st-3rd charge/discharge curves and (G) cycling performance at 0.1 A/g of FeCo@PAZ-C. (H) galvanostatic charge/discharge curves for 1st-3rd, 50th and 100th at 0.1 A/g, (I) rate capability, and (J) long-term cyclability of ZCS@NC@C@rGO, ZCS@NC@C and ZCS@NC. This figure is quoted with permission from Ref.[132,133] Copyright 2024, 2023 Elsevier.

(494.8 mAh/g@0.2 A/g), CR (74.7%) and rate capability, compared with MnSe@C (230.9 mAh/g) and ZnSe@C (343.2 mAh/g), due to the contributory effects of flower like shape with hierarchical porosity and rich accessible metal active sites besides high electrical conductivity of FC and synergism of ZMS[120]. Controlled synthetic strategies enable the easy tuning of physicochemical merits of PMMA selenides as efficient anodes for commercialization of PIBs. N-doped carbon-based composite with FeCo nanoalloys (FeCo@PAZ-C) was constructed from MOF-template annealing and tested as a good PIB anode[132]. FeCo@PAZ-C had spherical nanoalloys core-nanosphere shell morphology, proved by SEM [Figure 13E], that enabled excellent initial SC (1,232.0 mAh/g@0.1 A/g), CE and CR (95%) [Figure 13F and G], due to its capability to boost K^+-ion storage by lowering its diffusion routes and increase electron mobility. Incorporation of PMMAs on both surface and interior of conductive materials needs to be further explored for improved K^+-ion storage. N-doped carbon (NC), resorcinol-formaldehyde-derived carbon (C) and rGO confined ZnSe/$Co_{0.85}$Se (ZCS@NC@C@rGO) was synthesized by co-precipitation/selenization/annealing

and examined as a good PIB anode[133]. The ZCS@NC@C@rGO had superior initial SC (422.2 mAh/g@0.1 A/g) to ZCS@NC (340 mAh/g) and ZCD@NC@C (345 mAh/g), besides its good rate capability and cycling performance [Figure 13H-J]. This was due to the porous carbon microcubes and carbon shell that provided rich channels for rapid electron mobility and K^+-ions intercalation/deintercalation and prevented agglomeration of the bimetallic selenides and volume change. Notably, multilevel spatial confinement of PMMA selenides is an efficient strategy to enhance the K^+-ion storage and stability.

Germanium-based alloy anodes (GeV_4S_8) were rationally fabricated by physical mixing/annealing to incorporate Ge atoms into V-S framework with loosely packed and metallic media that facilitated rapid K^+-ion/electron diffusion and reduced volume expansion, shown by theoretical calculations [Figure 14A-F], as a good PIB anode at SC (400.0 mAh/g@0.5 A/g), and CR (80%), compared to most state-of-the-art anodes[134]. The dual functions of multimetallic alloy selenides and fast K^+-ions intercalation enable high capacity and kinetics of PIB anodes. Vulcanization annealing was explored to incorporate CoS_2/SnS_2 into S-doped carbon (CoS_2/SnS_2@SC), which gave excellent K^+-ion storage at high initial discharge SC (1,026.0 mAh/g@0.1 A/g), CR (76%), and cycling performance[135]. This was due to the internal voids in the CoS_2/SnS_2 core and enhanced electron transport with alleviated polysulfide dissolution. Selective morphological and structural designs of multimetallic alloy anodes are significant for excellent K^+-ion storage. A 3D composite microsphere (CoFe)Se_x-rGO-CNT) was synthesized by spray pyrolysis and the effect of electrolyte (dimethyl ether (DME)- and ethylene carbonate (EC)/DEC-based) on its PIB anodic performance was explored[136]. The structural stability of (CoFe)Se_x-rGO-CNT allowed higher CE, rate capability, K^+ ions diffusion and cycling stability than (CoFe)Se_x-rGO, besides improved K^+-ion storage in DME-based electrolyte, relative to EC/DEC-based electrolyte. This was attributed to the formation of a thin stable solid-electrolyte layer (SEI) in DME-based electrolyte. Suitable electrolytes with appropriate SEI layers that allow rapid ions/electron transport are considerable parameters for the assembly of high-performance PIBs. A 3D microflower $BiFeO_3$ (BFO-MF), assembled from its nanosheets precursors via solvothermal method, exhibited impressive performance as a PIB anode at good SC (606.0 mAh/g), great cycling performance, CR (98.2%) and power/energy densities (2,152.8 W/kg; 177.1 Wh/kg)[137]. This was traced to its favorable affinity/diffusion for K^+-ions with rapid electrochemical kinetic and contracted voltage-hysteresis, proved by theoretical calculations [Figure 14G-J]. This work proposed the possibility of extensive research in developing advanced Bi-based alloy anodes for high ED and durable PIBs.

Solvothermal/calcination methods were explored for the construction of FeS_2/MoS_2 on N-doped carbon (FMS@NC) with spherical flower-like morphology, synergistic effect to alleviate volume expansion and conductivity to give good PIB anodic performance at SC (585.0 mAh/g@0.05 A/g), CR (93.9%) and cycling capability[138]. Systematic construction of heterostructure alloys with conductive materials is viable for high-performance PIB anodes and stability. Although PMMAs are promising anodes for PIBs, only very few studies have been reported as far as we found. The *in-situ* construction of PMMAs with Cu substrate revealed the best K^+-ion storage capacity and long-term durability. Thus, there is a need for this area of research to be extensively exploited and optimized.

RAMIBS RECYCLING AND CIRCULAR ECONOMY

The recycling of RAMIBs is pivotal for developing a sustainable circular economy, mitigating environmental hazards, and promoting a sustainable future, but it remains a significant challenge[139]. This is attributed to the complex chemistry and the need for specific processes to recover rare metals (i.e., Li, Ni, Al, and Co)[140,141], which offer an alternative way to decrease the consumption of these metals besides reducing wastes. Life cycle assessments, including all steps from the extraction of anode materials to end-of-life treatment, are needed to estimate the environmental footprint of RAMIBs recycling processes to determine areas that require prompt improvements to enhance sustainability[142]. For example, unveiling the

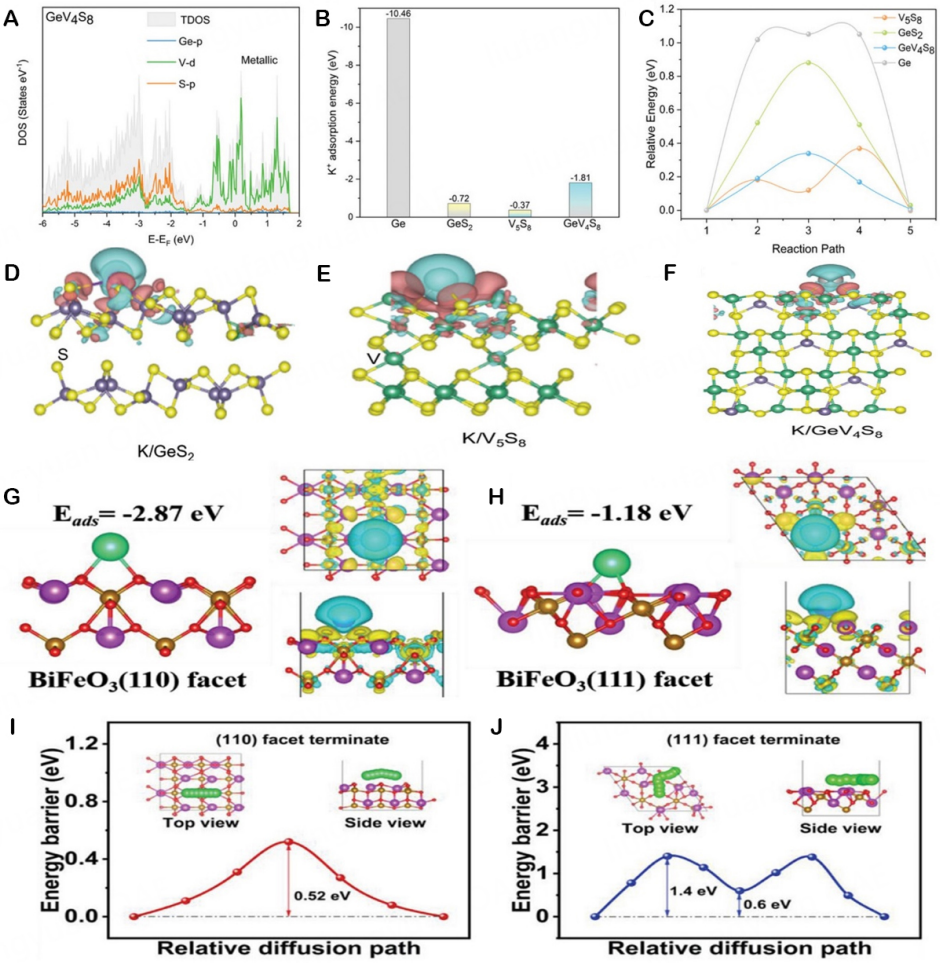

Figure 14. (A) Density of state (DOS), (B) K^+-ions adsorption energies, (C) K^+-ions diffusion energy barriers of GeV_4S_8, V_5S_8, GeS_2 and Ge, and (D-F) charge density difference maps with side views of K/GeV_4S_8, K/V_5S_8, and K/GeS_2. (G and H) Structural models and corresponding charge density differences for the adsorption of K^+ ions on {110} and {111} facets, (I and J) energy and diffusion barrier of $BiFeO_3$. This figure is reproduced with permission from Ref.[134,137] Copyright 2024 Wiley-VCH.

trade-offs between the environmental benefits of material recycling and the encumbrances of collection and treatment can direct the process towards more eco-friendly practices[142]. Also, the rational design of advanced recycling technologies and life cycle thinking in managing RAMIBs is vital to attain a circular economy[143-145].

Considering the widespread applications of the RAMIB devices for portable electronics, electric vehicles and renewable energy systems, their environmental impact assessment, including (i) raw materials mining and resources extraction; (ii) production stage; (iii) usage phase; and (iv) end of life and recycling, is a crucial area of concern. The extraction of the anode materials (Li, Na, K) from mineral ores and brine deposits could result in water depletion, contamination and environmental disorders. For instance, the mining of cobalt, manganese and nickel results in total emission of 8.1 $GtCO_2$ equivalent in 2050[146], which causes considerable environmental degradation, such as soil and water pollution, deforestation and harmful consequences on the immediate localities. Also, the manufacturing of RAMIBs (LIBs, SIBs and PIBs) requires high energy consumption, which contributes to greenhouse gas emissions and carbon footprint, which are highly concentrated in three countries: China (45%), Indonesia (13%) and Australia (9%)[146].

Besides, the use of various chemicals during the production of RAMIBs could pose the risks of hazardous chemical spillage and pollution if not optimally managed. However, during their use for electric vehicles and renewable energy systems, the RAMIBs are highly effective in reducing the overall greenhouse gas emissions, as no pollutants are emitted, making them cleaner than fossil fuel-based systems[147]. After complete usage (i.e., end of life stage), the RAMIBs are either disposed of or recycled: inappropriate disposal of the RAMIBs could result in water and soil pollution with toxic materials such as heavy metals and pose fire hazards with environmental and safety concerns; meanwhile recycling of valuable materials in spent RAMIBs is complex and not economically viable[148]. Hence, the current recycling rate of RAMIBs is extremely low. Significant enhancement of the technology and infrastructures is a necessity for sustainability. Although there are environmental concerns associated with the production of RAMIBs, the devices still significantly reduce the emissions of greenhouse gas by 38% in 2050[146], particularly for transportation and renewable energy systems. Their sustainability efforts are directed toward improving the RAMIB technology with much focus on reducing total reliance on essential raw materials, advancing recyclability and devising more mining sustainable and manufacturing processes, implementing stricter policy regulations, and promoting sustainable practices in the RAMIB lifecycle.

The policymakers who can promote a circular economy for RAMIBs recycling need proper and clear policy measures to drive sustainable practices and enhance resource efficiency through various processes[149]. This includes material management (i.e., supply chain traceability, material transport/storage/recovery), awareness (i.e., stakeholder engagement and educational campaigns), incentivizing circular business models (i.e., financial incentives, and market signals), and worldwide cooperation[149].

The market size and growth of RAMIBs recycling are noteworthy, indicating the growing importance of sustainability in the battery industry. Mainly, the global market size of battery recycling is nearly 1.83 billion USD in 2023 and is expected to grow by about 37.6% from 2024 to 2030[150]. The market share of RAMIBs is about 75% of the global battery market share[150]. Some successful examples of battery recycling occurred in China, which leads the global battery recycling with over 500,000 metric tons, compared with the USA and Europe, both of which had a recycling capacity of nearly 200,000 metric tons[151,152]. The leading technologies for recycling batteries in China include recycling electric-vehicle batteries and utilization of spent vehicle batteries, which could reach a market size of (3.59 billion Euros) by 2025, and reusing electric-vehicle batteries operate below 70%-80% capacity after 4-6 years in slower light electric vehicles and stationary energy storage application[153,154]. In Europe, the recycling market for batteries will reach 130GWh by 2030, which is about 700 kilotons of recycling capacity required, and will increase by three times by 2040[152].

CONCLUSION AND OUTLOOK

In brief, this article reviews the rational design of PMMA (i.e., Sn, Mn, Mo, Co, V, and Fe) anodes using various approaches (i.e., template-based, hydrothermal/solvothermal, chemical reduction, electrochemical deposition, sol-gel, dealloying and electrospinning) for the RAMIBs (i.e., LIBs, SIBs, and PIBs). This is besides the fundamental aspects (i.e., mechanisms and calculations), along with the deep discussions on the key descriptive factors of RAMIBs (i.e., lifespans, ED, structural changes, and mechanisms) corroborated with the summary tables, schemes, and figures. The results discussed above warranted that the performance of PMMAs in LIBs is significantly superior to SIBs and PIBs, respectively, as shown in the higher SC, CR and cycling durability [Tables 1-3]. Meanwhile, the most active anodes in LIBs were $FeCo_2O_4$ octahedral (SC = 2,436@0.2 A/g) prepared by the sol-gel method[69], 3D reticular-like and $ZnMn_2O_4$/NF (SC = 2,211@0.4 A/g) obtained using hard-template/annealing[87], $FeCo_2O_4$ (SC = 2,436@0.2 A/g), and $CoFe_2O_4$ nanoplates (SC = 2,134.7@0.1 A/g) by melt spinning/dealloying[99]. The sol-gel method is the most promising for tailoring morphology and compositions of RAMIBs. Despite the advances in PMMA anodes

Table 1. Comparative porous transition metal alloy anodes for LIBs

Anodes	Synthesis method	Morphology	Electrolyte	Capacity/mAh/g@current density (A/g)	Cycles	Capacity retention/%	Ref.
Sn/Cu foam	Electrodeposition	Grape-like foam	1 M $LiPF_6$ in EC/DMC (1:1)	821.5@0.1	50	58.0	[56]
Sn-Sb/Cu	Template-like electrodeposition/annealing	Sponge-like foam	1 M $LiPF_6$ in EC/DMC/DEC (1:1:1)	651.9@0.5	30	82.9	[57]
ATO/N-GCA	Hydrothermal	Spherical metals on sheet-like nanotube	1 M $LiPF_6$ in EC/DMC (1:1)	942@1.0	1,000	72.7	[58]
$CoSn_2$	Chemical reduction	Tetragonal	1 M $LiPF_6$ in EC/DMC (1:1)/FEC(3%)	650@2.0	5,000	-	[59]
$CoSn_2O_x$	Chemical reduction/ball milling	Spherical	1 M $LiPF_6$ in EC/DMC (1:1)	525@2.0	1,500	92.0	[60]
rGO/$NiCo_2O_4$	Hydrothermal/annealing	Nanosheets on porous wrinkled films	1 M $LiPF_6$ in EC/DMC (1:1)	1,697.9@0.2	50	61.0	[65]
CuO/CoO core/shell array on Cu foam	Hard-template and annealing	Nanosheets on nanotubes	1 M $LiPF_6$ in EC/DMC/DEC (1:1:1)	1,216@0.1	1,000	93.8	[66]
$ZnCo_2O_4$/NF	Hard template/calcination	Flower-like nanosheets	1 M $LiPF_6$ in EC/DMC/EMC (1:1:1)	1,544@0.1	100	82.0	[67]
$NiCo_2O_4$/NiO-HD	Solvothermal/calcination	Hollow dodecahedron	1 M $LiPF_6$ in EC/DMC (1:1)	1,622@0.2	100	63.5	[32]
$NiCo_2O_4$	Solvothermal/annealing	Rose flower-like nanosheets	1 M $LiPF_6$ in EC/DEC (1:1)	1,282@1.0	100	94.0	[68]
$FeCo_2O_4$	Sol-gel/annealing	Octahedral	1 M $LiPF_6$ in EC/DMC/DEC (1:1:1)	2,436@0.2	200	95.2	[69]
ZNCO/GNS	Hard-template/calcination/chemicalreduction	Microspheres core/nanosheet shell	1 M $LiPF_6$ in EC/DMC/EMC (1:1:1)	1,429@0.1	50	95.0	[70]
$ZnCo_2O_4$ film/NF	Hard-template/annealing	3D porous networks	1 M $LiPF_6$ in EC/DEC (1:1)	1,726@0.4	100	63.0	[71]
Te@$ZnCo_2O_4$	Templated/annealing	Core-shell nanofibers	1 M $LiPF_6$ in EC/DEC (1:1)	1,364@0.1	100	~100	[72]
Zn-Co-S@NS-CP	Template pyrolysis	Hollow polyhedron	1 M $LiPF_6$ in EC/DMC/DEC (1:1:1)	1,298.1@0.57	400	-	[73]
CoO-ZnO@NC-450	Hydrothermal/annealing	Spherical nanoparticles	1 M $LiPF_6$ in EC/DMC (1:1)	975.2@0.2	100	81.6	[74]
$CoMoO_4$-CoO/S@rGO	Templated hydrothermal/Annealing	Spherical metals on polyhedron sheets	1 M $LiPF_6$ in EC/DEC (1:1)/FEC (5 wt.%)	1,672@0.5	150	62.1	[75]
CoO/Cu	Hard-template/pulsed electrodeposition	Nanowire core/spherical shell	1 M $LiPF_6$ in EC/DEC (1:1)	1,215@0.5	250	68.1	[76]
$ZnMn_2O_4$	solvothermal/annealing	Twin-microspheres	1 M $LiPF_6$ in EC/DMC/DEC (1:1:1)	1,106@0.5	130	77.8	[84]
$ZnMnO_3$	Co-precipitation/annealing	Spherulites	1 M $LiPF_6$	1,294@0.5	150	67.9	[85]
$CoMn_2O_4$/NF	Hard-template/annealing	3D reticular-like	1 M $LiPF_6$ in EC/DMC (1:1)	1,833@0.4	100	74.5	[86]
$ZnMn_2O_4$/NF	Hard-template/annealing	3D reticular-like	1 M $LiPF_6$ in EC/DMC (1:1)	2,211@0.4	100	94	[87]
Ni-Co-Mn oxide QS-HS	Self-templated hydrothermal/annealing	Hollow microspheres	1 M $LiPF_6$ in EC/DMC (1:1)	1,761.8@0.2	250	79.5	[88]

np-Ni@NiO/MnO/NF	Induction melting/dealloying/annealing	Coarsened grains	1 M $LiPF_6$ in EC/DMC/DEC (1:1:1)	960@0.1	200	105	[89]
ZMO-G500	Solvothermal/calcination	Spherical metal on nanosheets	1 M $LiPF_6$ in EC/DMC (1:1)	1,100@0.1	200	99.95%	[90]
MN-1/P	*In-situ* electroconversion/calcination	Flower-like nanosheets	1 M $LiPF_6$ in EC/DMC (1:1)	1,554@0.1	1,000	~100	[91]
Cu/Mn_3O_4@SC	Template annealing	Microspheres	1 M $LiPF_6$ in EC/DEC (1:1)	766.2@0.2	1,000	66.3	[92]
TFCs	Hydrothermal/calcination	Spherical metals on nanotubes	1 M $LiPF_6$ in EC/DMC/DEC (1:1:1)	1,589@0.5	450	58.0	[96]
3D-OHP-a-VO_x/MoO_y	Freeze-dried/annealing	(3D) ordered hierarchical porous sheets	1 M $LiPF_6$ in EC/DMC/DEC (1:1:1)	1,705@0.1	50	82.1	[97]
$Zn_3V_2O_8$	Solvothermal/annealing	Hollow nanocages	1 M $LiPF_6$ in EC/DMC/DEC (1:1:1)	1,906@0.1	200	70.7	[98]
$CoFe_2O_4$	Melt spinning/dealloying	Nanoplates	1 M $LiPF_6$ in EC/DMC (1:1)	2,134.7@0.1	200	99.1	[99]
NFO@C	Electrospinning/annealing	Spherical metals on fibers	1 M $LiPF_6$ in EC/DMC/DEC (1:1:1)	1,030@0.1	100	72.3	[100]
$Ni_3ZnC_{0.7}$	Evaporation-solidification/annealing	Irregular spheres	1 M $LiPF_6$ in EC/DEC (1:1)	1,100@0.05	1,000	100	[101]
$NiSi_x$/Si/C	Ball milling/annealing	Irregular spheres	1 M $LiPF_6$ in EC/EMC (1:1)	1,060@0.1	200	72	[102]
NiFe-$NiFe_2O_4$/rGO-8	Chemical reduction/annealing	Spherical metals on wrinkled sheets	1 M $LiPF_6$ in EC/DMC (1:1)	1,362@0.1	130	79.4	[103]
NiO/Co_3O_4/Fe_3O_4	Precipitation/calcination	Hollow nanocages	1 M $LiPF_6$ in EC/DMC/EMC (1:1:1)	1,052@0.5	400	85.7	[104]
$NiCo_2O_4$@Fe_2O_3	Hydrothermal/calcination	Flower-like porous channels	1 M $LiPF_6$ in EC/DEC (1:1)	1,640@1.0	400	57.6	[105]
$CoNiSe_2$/C-700	Template annealing	Nanododecahedral	1 M $LiPF_6$	2,125.5@0.1	1,000	98	[106]

EC: Ethylene carbonate; DEC: diethylene carbonate; FEC: fluoroethylene carbonate; Fe_xO_y/TFCs: TiO_2-modified iron oxides/carbon nanotubes; DMC: dimethylene carbonate; EMC: ethylene methyl carbonate; NF: nickel foam; MWCNTs: multi-walled carbon nanotubes; GNS: graphene nanosheets; CBD: chemical bath deposition.

for the RAMIBs, the current challenges could be thwarted via the following proposed potential research directions [Figure 15]:

• Many studies have addressed storage mechanisms, but PMMA anode failure mechanisms in RAMIBs are rarely reported, necessitating further investigation alongside ambiguous dendrite suppression and related chemical reactions[27]. This goal can be achieved by initially examining electrochemical merits of custom full cells, using experimental, theoretical, and *in-situ* studies to address problems in future electrode design[21].

• The preference for synergetic or strain effects in PMMAs, particularly with active alkali metals, remains unclear. Some reports indicate that synergism can enhance electrode durability and capacity[27]. Systematic studies, proper metal selection, and *in-situ* characterization techniques [TEM, XRD, X-ray photoelectron spectroscopy (XPS)] are essential to determine the preferred effect and monitor structural changes during the electrochemical reactions.

Table 2. Comparative porous transition metal alloy anodes for SIBs

Anodes	Synthesis method	Morphology	Electrolytes	Capacity/mAh/g@current density (A/g)	Cycles	Capacity retentio/%	Ref.
ATO/N-GCA	Hydrothermal	Spherical metals on sheet-like nanotubes	1 M $NaClO_4$ in EC/FEC (1:1)/FEC(5%)	409@0.1	500	74.0	[58]
SnSb/N-PCNWs	Electrospinning/annealing	Spherical metals in nanofibers	1 M $NaClO_4$ in EC/DMC (1:1)/	400@0.05	10,000	100	[117]
$SnSe_2$/$CoSe_2$@C	Selenization/carbonization	Nanobox core/shell	1 M $NaPF_6$ in DIGLYME/DOL (1:1)	455@0.1	500	77.6	[118]
Sn-Bi@C	Hydrothermal/annealing	nanosphere core-shell on layer support	1 M $NaPF_6$ in DME	462@0.1	2,000	86.9	[119]
ZMS@FC	Solvothermal/calcination	Flower-like metals on porous flakes	1 M SHCF in DEGDME	494.8@0.2	1,000	74.7	[120]
$Cu_4Mo_6Se_8$/C	Chelation/annealing	Ultrathin nanosheets polyhedral C skeleton	1 M $NaPF_6$ in DME	514@0.5	2,400	107.7	[121]
$CoSb_2Se_4$@Sb_2Se_3	Hydrothermal	Rod-shaped	1 M $NaCF_3SO_3$ in DEGDME	437.9@0.1	160	81.4	[122]
$NiCoSe_2$@NSC	Chemical reduction/annealing	Spherical nanoparticles on porous nanosheets	1 M $NaPF_6$ in DME	572.5@0.2	1,000	85.1	[123]
VS_4/SnS_2@MXene	Hydrothermal/etching/self-assembly	Nanosheets on layered MXene	1 M $NaPF_6$ in EC/DEC (1:1)/FEC(5%)	2,508.4@0.1	200	82.8	[124]
Mn-NiCoS-10	Solvothermal/annealing	Nanosheets	1 M $NaPF_6$ in DME	662.6@0.3	1,000	85.4	[125]

SHCF: Sodium hexacyanoferrate; DEGDME: diethylene glycol dimethyl ether; FEC: fluoroethylene carbonate; PEC: propylene carbonate; DIGLYME: diethylene glycol dimethyl ether; DOL: 1,3-dioxolane; $NaCF_3SO_3$: sodium trifluoromethylsulfonate.

• Current fabrication methods face barriers such as hazardous chemicals, low yield, and complexity, necessitating new green and simple synthesis methods for atomic-level metal mixing and improved surface features and structure stability[155,156].

• To optimize the performance of PMMA anodes, factors such as electrolyte type, additives, pH, and composition must be considered. Exploring cost-effective and durable electrolytes is crucial, with ionic liquid electrolytes and solid electrolytes being the most promising options[157,158]. Electrochemical impedance spectroscopy (EIS) analysis can estimate electrolyte resistance and provide insights on interfacial interactions[159].

• Interfacial engineering enhances kinetics and chemical durability in alkali metal ions intercalation/deintercalation[25]. Hierarchical porous morphologies with a high surface area-to-volume ratio and support materials, including carbon, improve metal dispersion and stability against aggregation[15,160,161]. Support can be optimized via *in-situ* fabrication of PMMAs with strong metal-support interaction.

Table 3. Comparative porous multimetallic alloy anodes for PIBs

Anodes	Synthesis method	Morphology	Electrolytes	Capacity/mAh/g@current density (A/g)	Cycles	Capacity retention/%	Ref.
NPCuBi	Melt-spinning/chemical dealloying	Nanospheres with bicontinuous open channel	1 M KFSI in DME	1,045@0.05	50	> 93.0	[131]
ZMS@FC	Solvothermal/calcination	Flower-like metals on porous flakes	1 M KPF6 in EC/DEC (1:1)	494.8@0.2	1,000	74.7	[120]
FeCo@PAZ-C	Template/annealing	Spherical nanoparticle core on nanosphere shell	1 M KPF_6	1,232.0@0.1	500	95	[132]
ZnSe/Co0.85Se@NC@C@rGO	Co-precipitation/selenization/annealing	Microcubic core-shell	1 M KFSI in DME	422.2@0.1	2,000	55.5	[133]
GeV_4S_8	Physical mixing/annealing	Nanocubes	3 M KFSI in DME	400.0@0.5	1,000	80.0	[134]
CoS_2/SnS_2@SC	Vulcanization annealing	Core-shell	1.5 M KFSI in EC/DEC (1:1)	1,026.0@0.1	1,500	76.0	[135]
(CoFe)Se_x-rGO-CNT	Spray pyrolysis	Microspheres on hierarchical supports	1 M KFSI in EC/DEC	600.0@0.5	200	90.0	[136]
$BiFeO_3$-MF	Hydrothermal	Flower-like spheres	3 M KFSI in DME	606.0@0.5	5,000	98.2	[137]
FMS@NC	Solvothermal/calcination	Spherical flower-like	1.5 M KFSI in EC/DEC (1:1)	585.0@0.05	3,000	93.9	[138]

KFSI: Potassium bis(fluorosulfonyl)imide; DME: dimethyl ether.

• Encapsulation of low-temperature liquid MAs inside porous MA under high pressure offers a self-healing anode or substrate, preventing dendritic growth of alkali metals. However, new assembly approaches and electrolytes are required[162].

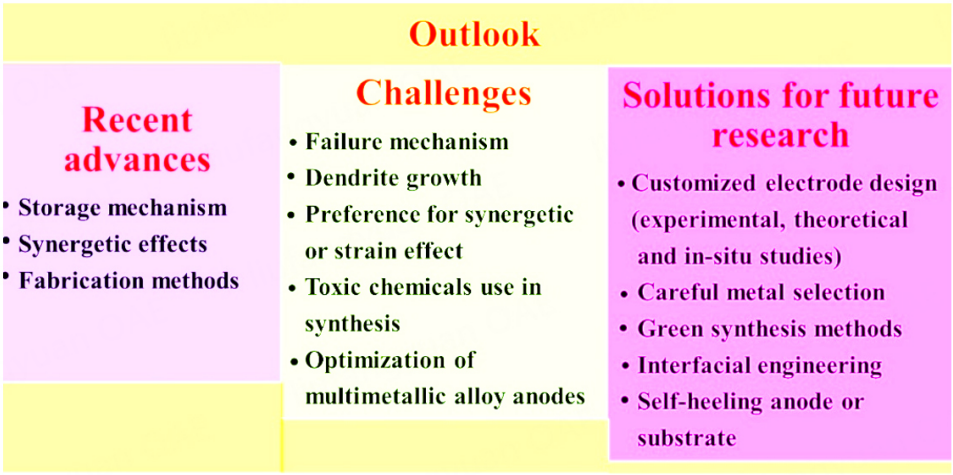

Figure 15. Summary of the outlook highlighting the recent advances, challenges and solutions proffered for future research.

DECLARATIONS

Authors' contributions

Data collection and writing: Ipadeola AK
Conceptualization, writing, and supervision: Eid K
Review, supervision, and funding: Abdullah AM

Availability of data and materials

The materials are available upon request.

Financial support and sponsorship

This work was supported by (i) the Qatar National Research Fund (QNRF, a Division of the QRDI Council) through the Academic Research Grant (ARG) program, Grant# ARG01-0524-230330, and (ii) Qatar University through an International Research Collaboration Co-Fund program, Grant# IRCC-2023-157.

Conflicts of interest

All authors declared that there are no conflicts of interest.

Ethical approval and consent to participate

Not applicable.

Consent for publication

Not applicable.

REFERENCES

1. Eid K, Gamal A, Abdullah AM. Graphitic carbon nitride-based nanostructures as emergent catalysts for carbon monoxide (CO) oxidation. *Green Chem* 2023;25:1276-310. DOI
2. Yu Y, Lv Z, Liu Z, et al. Activation of Ga liquid catalyst with continuously exposed active sites for electrocatalytic C-N coupling. *Angew Chem Int Ed* 2024;136:e202402236. DOI
3. Lu Q, Zhao X, Luque R, Eid K. Structure-activity relationship of tri-metallic Pt-based nanocatalysts for methanol oxidation reaction.

Coordin Chem Rev 2023;493:215280. DOI

4. Abdelgawad A, Salah B, Lu Q, et al. Template-free synthesis of M/g-C_3N_4 (M = Cu, Mn, and Fe) porous one-dimensional nanostructures for green hydrogen production. *J Electroanal Chem* 2023;938:117426. DOI
5. Gu Y, Nie N, Liu J, et al. Enriching H_2O through boron nitride as a support to promote hydrogen evolution from non-filtered seawater. *EcoEnergy* 2023;1:405-13. DOI
6. Liu H, Li J, Arbiol J, Yang B, Tang P. Catalytic reactivity descriptors of metal-nitrogen-doped carbon catalysts for electrocatalysis. *EcoEnergy* 2023;1:154-85. DOI
7. Yu W, Huang H, Qin Y, et al. The synergistic effect of pyrrolic-N and pyridinic-N with Pt under strong metal-support interaction to achieve high-performance alkaline hydrogen evolution. *Adv Energy Mater* 2022;12:2200110. DOI
8. Lu Q, Li J, Eid K, et al. Facile one-step aqueous-phase synthesis of porous PtBi nanosponges for efficient electrochemical methanol oxidation with a high CO tolerance. *J Electroanal Chem* 2022;916:116361. DOI
9. Ganesan V, Kim DH, Park CM. Robust CoP_2-C hollow nanoboxes: superior anodes for Li- and Na-ion batteries. *J Energy Stor* 2024;79:110197. DOI
10. Nam KH, Ganesan V, Kim DH, Jeong S, Jeon KJ, Park CM. $SiSe_2$ for superior sulfide solid electrolytes and Li-ion batteries. *ACS Appl Mater Interfaces* 2024;16:643-54. DOI
11. Tian H, Song A, Tian H, et al. Single-atom catalysts for high-energy rechargeable batteries. *Chem Sci* 2021;12:7656-76. DOI PubMed PMC
12. Peng Q, Rehman J, Eid K, et al. Vanadium Carbide (V_4C_3) MXene as an efficient anode for Li-ion and Na-ion batteries. *Nanomaterials* 2022;12:2825. DOI PubMed PMC
13. Ma F, Liu Y, Huang T, Du X, Lu Q, Kid K. Facile in situ polymerization synthesis of poly(ionic liquid)-based polymer electrolyte for high-performance solid-state batteries. *Energy Convers Manag X* 2024;22:100570. DOI
14. Wu J, Chen X, Fan W, Li X, Mai Y, Chen Y. Rationally designed alloy phases for highly reversible alkali metal batteries. *Energy Stor Mater* 2022;48:223-43. DOI
15. Ganesan V, Lee Y, Jung H, Park C. Porous polyhedral carbon matrix for high-performance Li/Na/K-ion battery anodes. *Carbon Lett* 2023;33:2189-98. DOI
16. Kim Y, Kim K, Seo H, Lee S, Park C, Kim J. Surfactant-derived porous $Sn_2Nb_2O_7$-graphene oxide composite as Li- and Na-ion storage materials. *J Alloys Compd* 2022;910:164943. DOI
17. Kim T, Jeon K, Park C. Black P@MO (M = Mg, Al, or Ti) composites as superior Li-ion battery anodes. *Chem Eng J* 2021;424:130366. DOI
18. Glushenkov A. Recent commentaries on the expected performance, advantages and applications of sodium-ion batteries. *Energy Mater* 2023;3:300010. DOI
19. Tian H, Tian H, Yang W, et al. Stable hollow-structured silicon suboxide-based anodes toward high-performance lithium-ion batteries. *Adv Funct Mater* 2021;31:2101796. DOI
20. Ma Z, Song A, Liu Z, et al. Nanoconfined expansion behavior of hollow MnS@Carbon anode with extended lithiation cyclic stability. *Adv Funct Mater* 2023;33:2301112. DOI
21. Qi S, Deng J, Zhang W, Feng Y, Ma J. Recent advances in alloy-based anode materials for potassium ion batteries. *Rare Met* 2020;39:970-88. DOI
22. Wang J, Wang Y, Zhang P, Zhang D, Ren X. Preparation and electrochemical properties of binary SixSb immiscible alloy for lithium ion batteries. *J Alloy Compd* 2014;610:308-14. DOI
23. Li G, Guo S, Xiang B, et al. Recent advances and perspectives of microsized alloying-type porous anode materials in high-performance Li- and Na-ion batteries. *Energy Mater* 2022;2:200020. DOI
24. Shao Y, Jin Z, Li J, Meng Y, Huang X. Evaluation of the electrochemical and expansion performances of the Sn-Si/graphite composite electrode for the industrial use. *Energy Mater* 2022;2:200004. DOI
25. Pathak AD, Chanda UK, Samanta K, Mandal A, Sahu KK, Pati S. Selective leaching of Al from hypereutectic Al-Si alloy to produce nano-porous silicon (NPS) anodes for lithium ion batteries. *Electrochim Acta* 2019;317:654-62. DOI
26. Zhang M, Mou X, Zhou X, Wang J, Li H, Wang C. Metal compound-based heterostructures in anodes promote high capacity and fast reaction kinetic for lithium/sodium-ion storage: a review. *ChemElectroChem* 2024;11:e202300573. DOI
27. Wang X, Tang S, Guo W, Fu Y, Manthiram A. Advances in multimetallic alloy-based anodes for alkali-ion and alkali-metal batteries. *Materi Today* 2021;50:259-75. DOI
28. Pirayesh P, Tantratian K, Amirmaleki M, et al. From nanoalloy to nano-laminated interfaces for highly stable alkali-metal anodes. *Adv Mater* 2023;35:e2301414. DOI
29. Liu J, Wang J, Xu C, et al. Advanced energy storage devices: basic principles, analytical methods, and rational materials design. *Adv Sci* 2018;5:1700322. DOI PubMed PMC
30. Ipadeola AK, Eid K, Abdullah AM. Porous transition metal-based nanostructures as efficient cathodes for aluminium-air batteries. *Curr Opin Electroche* 2023;37:101198. DOI
31. Ipadeola AK, Haruna AB, Gaolatlhe L, et al. Efforts at enhancing bifunctional electrocatalysis and related events for rechargeable zinc-air batteries. *ChemElectroChem* 2021;8:3998-4018. DOI
32. Sun C, Yang J, Rui X, et al. MOF-directed templating synthesis of a porous multicomponent dodecahedron with hollow interiors for enhanced lithium-ion battery anodes. *J Mater Chem A* 2015;3:8483-8. DOI

33. Su Z, Chen T. Porous Noble metal electrocatalysts: synthesis, performance, and development. *Small* 2021;17:e2005354. DOI PubMed
34. Tang J, Xu J, Ye Z, et al. Synthesis of flower-like cobalt, nickel phosphates grown on the surface of porous high entropy alloy for efficient oxygen evolution. *J Alloy Compd* 2021;885:160995. DOI
35. Adegoke KA, Maxakato NW. Porous metal oxide electrocatalytic nanomaterials for energy conversion: oxygen defects and selection techniques. *Coord Chem Rev* 2022;457:214389. DOI
36. Sahoo DP, Das KK, Mansingh S, Sultana S, Parida K. Recent progress in first row transition metal Layered double hydroxide (LDH) based electrocatalysts towards water splitting: a review with insights on synthesis. *Coord Chem Rev* 2022;469:214666. DOI
37. Mofokeng TP, Ipadeola AK, Tetana ZN, Ozoemena KI. Defect-engineered nanostructured Ni/MOF-derived carbons for an efficient aqueous battery-type energy storage device. *ACS Omega* 2020;5:20461-72. DOI PubMed PMC
38. Salah B, Ipadeola AK, Khan A, et al. Unveiling the electrochemical CO oxidation activity on support-free porous PdM (M = Fe, Co, Ni) foam-like nanocrystals over a wide pH range. *Energy Convers Manag* 2023;20:100449. DOI
39. Ipadeola AK, Abdelgawad A, Salah B, et al. Self-standing foam-like Pd-based alloys nanostructures for efficient electrocatalytic ethanol oxidation. *Int J Hydrogen Energy* 2023;48:30354-64. DOI
40. Salah B, Ipadeola AK, Abdullah AM, Ghanem A, Eid K. Self-standing Pd-based nanostructures for electrocatalytic CO oxidation: do nanocatalyst shape and electrolyte pH matter? *Int J Mol Sci* 2023;24:11832. DOI PubMed PMC
41. Lu S, Eid K, Lin M, Wang L, Wang H, Gu H. Hydrogen gas-assisted synthesis of worm-like PtMo wavy nanowires as efficient catalysts for the methanol oxidation reaction. *J Mater Chem A* 2016;4:10508-13. DOI
42. Airo MA, Otieno F, Mxakaza L, et al. Probing the stoichiometry dependent catalytic activity of nickel selenide counter electrodes in the redox reaction of iodide/triiodide electrolyte in dye sensitized solar cells. *RSC Adv* 2020;10:39509-20. DOI PubMed PMC
43. Navas D, Fuentes S, Castro-Alvarez A, Chavez-Angel E. Review on Sol-Gel synthesis of perovskite and oxide nanomaterials. *Gels* 2021;7:275. DOI PubMed PMC
44. He X, Liao J, Wang S, et al. From nanomelting to nanobeads: nanostructured Sb_xBi_{1-x} alloys anchored in three-dimensional carbon frameworks as a high-performance anode for potassium-ion batteries. *J Mater Chem A* 2019;7:27041-7. DOI
45. Parashar M, Shukla VK, Singh R. Metal oxides nanoparticles via sol-gel method: a review on synthesis, characterization and applications. *J Mater Sci Mater Electron* 2020;31:3729-49. DOI
46. Issa AA, El-Azazy M, Luyt AS. Kinetics of alkoxysilanes hydrolysis: an empirical approach. *Sci Rep* 2019;9:17624. DOI PubMed PMC
47. Danks AE, Hall SR, Schnepp Z. The evolution of 'sol-gel' chemistry as a technique for materials synthesis. *Mater Horiz* 2016;3:91-112. DOI
48. Subbiah T, Bhat GS, Tock RW, Parameswaran S, Ramkumar SS. Electrospinning of nanofibers. *J Appl Polym Sci* 2005;96:557-69. DOI
49. Paul D, Robeson L. Polymer nanotechnology: nanocomposites. *Polymer* 2008;49:3187-204. DOI
50. Huang C, Thomas N. Fabricating porous poly(lactic acid) fibres via electrospinning. *Eur Polym J* 2018;99:464-76. DOI
51. Sun B, Long Y, Zhang H, et al. Advances in three-dimensional nanofibrous macrostructures via electrospinning. *Prog Polym Sci* 2014;39:862-90. DOI
52. Liao Y, Loh C, Tian M, Wang R, Fane AG. Progress in electrospun polymeric nanofibrous membranes for water treatment: Fabrication, modification and applications. *Prog Polym Sci* 2018;77:69-94. DOI
53. Ni J, Zhu X, Yuan Y, et al. Rooting binder-free tin nanoarrays into copper substrate via tin-copper alloying for robust energy storage. *Nat Commun* 2020;11:1212. DOI PubMed PMC
54. Huang B, Pan Z, Su X, An L. Tin-based materials as versatile anodes for alkali (earth)-ion batteries. *J Power Sources* 2018;395:41-59. DOI
55. Mou H, Xiao W, Miao C, Li R, Yu L. Tin and Tin compound materials as anodes in lithium-ion and sodium-ion batteries: a review. *Front Chem* 2020;8:141. DOI PubMed PMC
56. Nam DH, Kim RH, Han DW, Kwon HS. Electrochemical performances of Sn anode electrodeposited on porous Cu foam for Li-ion batteries. *Electrochimica Acta* 2012;66:126-32. DOI
57. Zhao H, Zhang G, Jiang C, He X. An electrochemical and structural investigation of porous composite anode materials for LIB. *Ionics* 2012;18:11-8. DOI
58. Cui J, Yao S, Huang J, et al. Sb-doped SnO_2/graphene-CNT aerogels for high performance Li-ion and Na-ion battery anodes. *Energy Stor Mater* 2017;9:85-95. DOI
59. Wang S, He M, Walter M, Krumeich F, Kravchyk KV, Kovalenko MV. Monodisperse $CoSn_2$ and $FeSn_2$ nanocrystals as high-performance anode materials for lithium-ion batteries. *Nanoscale* 2018;10:6827-31. DOI
60. Walter M, Doswald S, Krumeich F, et al. Oxidized Co-Sn nanoparticles as long-lasting anode materials for lithium-ion batteries. *Nanoscale* 2018;10:3777-83. DOI
61. Li Z, Xue H, Wang J, Tang Y, Lee C, Yang S. Reduced graphene oxide/marcasite-type cobalt selenide nanocrystals as an anode for lithium-ion batteries with excellent cyclic performance. *ChemElectroChem* 2015;2:1682-6. DOI
62. Han Z, Wang B, Liu X, Wang G, Wang H, Bai J. Peapod-like one-dimensional (1D) CoP hollow nanorods embedded into graphene networks as an anode material for lithium-ion batteries. *J Mater Sci* 2018;53:8445-59. DOI
63. Cui C, Wei Z, Zhou G, et al. Quasi-reversible conversion reaction of $CoSe_2$/nitrogen-doped carbon nanofibers towards long-lifetime

anode materials for sodium-ion batteries. *J Mater Chem A* 2018;6:7088-98. DOI

64. Dong W, Shen D, Yang S, et al. First-principles Study of Mechanical and Electronic Properties of Co-Sn Intermetallics for Lithium Ion Battery Anode. *Chem Res Chin Univ* 2018;34:235-40. DOI
65. Gao G, Wu HB, Lou XW. Citrate-assisted growth of $NiCo_2O_4$ nanosheets on reduced graphene oxide for highly reversible lithium storage. *Adv Energy Mater* 2014;4:1400422. DOI
66. Wang J, Zhang Q, Li X, Zhang B, Mai L, Zhang K. Smart construction of three-dimensional hierarchical tubular transition metal oxide core/shell heterostructures with high-capacity and long-cycle-life lithium storage. *Nano Energy* 2015;12:437-46. DOI
67. Zhang Q, Wang J, Dong J, et al. Facile general strategy toward hierarchical mesoporous transition metal oxides arrays on three-dimensional macroporous foam with superior lithium storage properties. *Nano Energy* 2015;13:77-91. DOI
68. Xu J, Su D, Bao W, Zhao Y, Xie X, Wang G. Rose flower-like $NiCo_2O_4$ with hierarchically porous structures for highly reversible lithium storage. *J Alloys Compd* 2016;684:691-8. DOI
69. Zhu H, Sun Y, Zhang X, Tang L, Guo J. Evaporation-induced self-assembly synthesis of mesoporous $FeCo_2O_4$ octahedra with large and fast lithium storage properties. *Mater Lett* 2016;166:1-4. DOI
70. Zhang Q, Chen H, Han X, et al. Graphene-encapsulated nanosheet-assembled zinc-nickel-cobalt oxide microspheres for enhanced lithium storage. *ChemSusChem* 2016;9:186-96. DOI
71. Yuan J, Chen C, Hao Y, et al. A facile synthetic strategy to three-dimensional porous $ZnCo_2O_4$ thin films on Ni foams for high-performance lithium-ion battery anodes. *J Electroanal Chem* 2017;787:158-62. DOI
72. Huang G, Li Q, Yin D, Wang L. Hierarchical porous Te@$ZnCo_2O_4$ nanofibers derived from Te@Metal-organic frameworks for superior lithium storage capability. *Adv Funct Mater* 2017;27:1604941. DOI
73. Tong H, Gong Z, Huang Y, et al. Bimetallic zinc-cobalt sulfides embedded within N, S-codoped hollow carbon polyhedra for superior lithium-ion batteries. *Appl Surf Sci* 2024;652:159233. DOI
74. Liu Y, Wang L, Chen G, et al. Nitrogen-containing bimetal oxides derived from cobalt-zinc MOF as anode materials for lithium-ion batteries. *J Phys Chem Solids* 2024;185:111728. DOI
75. Chen J, Zhu K, Liang P, et al. Ultrahigh reversible lithium storage of hierarchical porous Co-Mo oxides *via* graphene encapsulation and hydrothermal S-doping. *J Mater Chem A* 2022;10:5373-80. DOI
76. Chen M, Zhou W, Qi M, Zhang J, Yin J, Chen Q. Reconstruction of copper shell on metal oxides as enhanced nanoarrays electrodes for lithium ion batteries. *Mater Res Bull* 2017;86:308-12. DOI
77. Kamran U, Park S. Hybrid biochar supported transition metal doped MnO_2 composites: efficient contenders for lithium adsorption and recovery from aqueous solutions. *Desalination* 2022;522:115387. DOI
78. Gu X, Yue J, Li L, Xue H, Yang J, Zhao X. General Synthesis of MnOx (MnO_2, Mn_2O_3, Mn_3O_4, MnO) hierarchical microspheres as lithium-ion battery anodes. *Electrochim Acta* 2015;184:250-6. DOI
79. Feng L, Xuan Z, Zhao H, et al. MnO_2 prepared by hydrothermal method and electrochemical performance as anode for lithium-ion battery. *Nanoscale Res Lett* 2014;9:290. DOI PubMed PMC
80. Ashokkumar K, Dhanapandian S, Suthakaran S, Krishnakumar N, Anandan M. Synthesis of MnO_2 nanoparticles and its effective utilization as high-performance of supercapacitor. *Mater Today Proc* 2022;49:2675-8. DOI
81. Jiang H, Hu Y, Guo S, Yan C, Lee PS, Li C. Rational design of MnO/carbon nanopeapods with internal void space for high-rate and long-life Li-ion batteries. *ACS Nano* 2014;8:6038-46. DOI
82. Yue J, Gu X, Chen L, et al. General synthesis of hollow MnO_2, Mn_3O_4 and MnO nanospheres as superior anode materials for lithium ion batteries. *J Mater Chem A* 2014;2:17421-6. DOI
83. Gu X, Yue J, Chen L, et al. Coaxial MnO/N-doped carbon nanorods for advanced lithium-ion battery anodes. *J Mater Chem A* 2015;3:1037-41. DOI
84. Liu Y, Bai J, Ma X, Li J, Xiong S. Formation of quasi-mesocrystal $ZnMn_2O_4$ twin microspheres via an oriented attachment for lithium-ion batteries. *J Mater Chem A* 2014;2:14236-44. DOI
85. Liu X, Zhao C, Zhang H, Shen Q. Facile synthesis of porous $ZnMnO_3$ spherulites with a high lithium storage capability. *Electrochim Acta* 2015;151:56-62. DOI
86. Yuan J, Chen C, Hao Y, et al. Three-dimensionally porous $CoMn_2O_4$ thin films grown on Ni foams for high-performance lithium-ion battery anodes. *J Mater Sci* 2017;52:5751-8. DOI
87. Yuan J, Chen C, Hao Y, et al. Fabrication of three-dimensional porous $ZnMn_2O_4$ thin films on Ni foams through electrostatic spray deposition for high-performance lithium-ion battery anodes. *J Alloy Compd* 2017;696:1174-9. DOI
88. Luo D, Deng YP, Wang X, et al. Tuning shell numbers of transition metal oxide hollow microspheres toward durable and superior lithium storage. *ACS Nano* 2017;11:11521-30. DOI
89. Zhang S, Zhang Z, Kang J, et al. Double-shelled nanoporous NiO nanocrystal doped MnO/Ni network for high performance lithium-ion battery. *Electrochim Acta* 2019;320:134542. DOI
90. Lee J, Seo S, Kim D. Hierarchical $Zn_{1.67}Mn_{1.33}O_4$/graphene nanoaggregates as new anode material for lithium-ion batteries. *Int J Energy Res* 2019;43:1735-46. DOI
91. Lin S, Zhang T. Electrochemical in-situ generation of Ni-Mn MOF nanomaterials as anode materials for lithium-ion batteries. *J Alloy Compd* 2023;942:168926. DOI
92. Miao X, Wang L, Shi Y, et al. Cu- and S-doped multielement composite Cu/Mn_3O_4@SC microspheres derived from bimetallic CuMn-MOF as anode materials for lithium-ion batteries. *J Mater Sci* 2024;59:3930-46. DOI

93. Zheng M, Tang H, Li L, et al. Hierarchically nanostructured transition metal oxides for lithium-ion batteries. *Adv Sci* 2018;5:1700592. DOI PubMed PMC
94. Lin D, Liu Y, Liang Z, et al. Layered reduced graphene oxide with nanoscale interlayer gaps as a stable host for lithium metal anodes. *Nat Nanotechnol* 2016;11:626-32. DOI
95. Mwonga PV, Ipadeola AK, Naidoo SR, Quandt A, Ozoemena KI. Annealing boosts the supercapacitive properties of molybdenum disulfide powder. *Electroanalysis* 2020;32:2642-9. DOI
96. Liu J, Qian D, Feng H, et al. Designed synthesis of TiO_2-modified iron oxides on/among carbon nanotubes as a superior lithium-ion storage material. *J Mater Chem A* 2014;2:11372. DOI
97. Zhao D, Qin J, Zheng L, Cao M. Amorphous vanadium oxide/molybdenum oxide hybrid with three-dimensional ordered hierarchically porous structure as a high-performance Li-ion battery anode. *Chem Mater* 2016;28:4180-90. DOI
98. Yin Z, Qin J, Wang W, Cao M. Rationally designed hollow precursor-derived $Zn_3V_2O_8$ nanocages as a high-performance anode material for lithium-ion batteries. *Nano Energy* 2017;31:367-76. DOI
99. Wang Z, Fei P, Xiong H, Qin C, Zhao W, Liu X. $CoFe_2O_4$ nanoplates synthesized by dealloying method as high performance Li-ion battery anodes. *Electrochim Acta* 2017;252:295-305. DOI
100. Dong T, Wang G, Yang P. Electrospun $NiFe_2O_4$@C fibers as high-performance anode for lithium-ion batteries. *Diam Relat Mater* 2017;73:210-7. DOI
101. Song H, Su J, Wang C. Vacancies revitalized $Ni_3ZnC_{0.7}$ bimetallic carbide hybrid electrodes with multiplied charge-storage capability for high-capacity and stable-cyclability lithium-ion storage. *ACS Appl Energy Mater* 2018;1:5008-15. DOI
102. Ruttert M, Siozios V, Winter M, Placke T. Synthesis and comparative investigation of silicon transition metal silicide composite anodes for lithium ion batteries. *Z Anorg Allg Chem* 2019;645:248-56. DOI
103. Chen H, Shen X, Xu K, et al. NiFe-$NiFe_2O_4$/rGO composites: controlled preparation and superior lithium storage properties. *J Am Ceram Soc* 2021;104:6696-708. DOI
104. Zheng G, Deng Y, Yu X, Song M. Fe-based frameworks in situ derived 3D Ni-Co-Fe nanocage TMO anode for LIB batteries. *Ionics* 2022;28:5489-98. DOI
105. Zheng G, Yu X, Huang X, Deng Y, Yuan Z, Song M. Construction of three-dimensional crumpled Ni-Co TMOs for electrochemical energy storage. *Electroanalysis* 2023;35:e202200480. DOI
106. Han Q, Zhang W, Zhu L, et al. MOF-derived bimetallic selenide $CoNiSe_2$ nanododecahedrons encapsulated in porous carbon matrix as advanced anodes for lithium-ion batteries. *ACS Appl Mater Interfaces* 2024;16:6033-47. DOI
107. Yu XY, Lou XW. Mixed metal sulfides for electrochemical energy storage and conversion. *Adv Energy Mater* 2018;8:1701592. DOI
108. Wang S, Fang Y, Wang X, Lou XWD. Hierarchical microboxes constructed by SnS nanoplates coated with nitrogen-doped carbon for efficient sodium storage. *Angew Chem Int Ed* 2019;58:760-3. DOI
109. Li W, Chou SL, Wang JZ, Kim JH, Liu HK, Dou SX. $Sn_{4+x}P_3$ @ amorphous Sn-P composites as anodes for sodium-ion batteries with low cost, high capacity, long life, and superior rate capability. *Adv Mater* 2014;26:4037-42. DOI PubMed
110. Ramireddy T, Xing T, Rahman MM, et al. Phosphorus-carbon nanocomposite anodes for lithium-ion and sodium-ion batteries. *J Mater Chem A* 2015;3:5572-84. DOI
111. Chen C, Fu K, Lu Y, et al. Use of a tin antimony alloy-filled porous carbon nanofiber composite as an anode in sodium-ion batteries. *RSC Adv* 2015;5:30793-800. DOI
112. Luo W, Shen F, Bommier C, Zhu H, Ji X, Hu L. Na-ion battery anodes: materials and electrochemistry. *ACC Chem Res* 2016;49:231-40. DOI
113. Zheng S, Tian Y, Liu Y, et al. Alloy anodes for sodium-ion batteries. *Rare Met* 2021;40:272-89. DOI
114. Wang X, Fan L, Gong D, Zhu J, Zhang Q, Lu B. Core-shell Ge@Graphene@TiO_2 nanofibers as a high-capacity and cycle-stable anode for lithium and sodium ion battery. *Adv Funct Mater* 2016;26:1104-11. DOI
115. Yue C, Yu Y, Sun S, et al. High performance 3D Si/Ge nanorods array anode buffered by TiN/Ti interlayer for sodium-ion batteries. *Adv Funct Mater* 2015;25:1386-92. DOI
116. Fang Y, Yu XY, Lou XWD. Formation of Hierarchical Cu-Doped $CoSe_2$ microboxes via sequential ion exchange for high-performance sodium-ion batteries. *Adv Mater* 2018;30:e1706668. DOI PubMed
117. Gu H, Yang L, Zhang Y, et al. Highly reversible alloying/dealloying behavior of SnSb nanoparticles incorporated into N-rich porous carbon nanowires for ultra-stable Na storage. *Energy Stor Mater* 2019;21:203-9. DOI
118. Zhang Y, Zhong W, Tan P, Niu Y, Zhang X, Xu M. Heterogeneous interface design of bimetallic selenide nanoboxes enables stable sodium storage. *Inorg Chem Front* 2021;8:4796-805. DOI
119. Chen J, Zhang G, Xiao J, et al. A stress self-adaptive bimetallic stellar nanosphere for high-energy sodium-ion batteries. *Adv Funct Mater* 2024;34:2307959. DOI
120. Zhou P, Zhang M, Wang L, et al. MOFs-derived flower-like hierarchically porous Zn-Mn-Se/C composite for extraordinary rate performance and durable anode of sodium-ion and potassium-ion batteries. *Small* 2022;18:e2203964. DOI
121. Wang S, Zou R, Liu Q, Chen H. Bimetallic selenide $Cu_4Mo_6Se_8$ nanosheet arrays grown on a carbon skeleton *via* MOF-derived with enhanced electrochemical kinetics for high-performance sodium-ion batteries. *J Mater Chem A* 2023;11:8710-8. DOI
122. Guo Y, Li X, Li Z, et al. Rational construction of Sb_2Se_3 wrapped bimetallic selenide as anode material toward efficient sodium storage performance. *Ceram Int* 2024;50:14959-67. DOI
123. Zhang L, Xie P, Zhang X, Zhu B, Liu T, Yu J. Facile synthesis of $NiCoSe_2$@carbon anode for high-performance sodium-ion

batteries. *J Colloid Interface Sci* 2024;662:1075-85. DOI

124. Hou YL, Chen JZ, Zhang BH, Wang HY, Wen WX, Zhao DL. Fast ion/electron transport enabled by MXene confined bimetallic sulfides with heterostructure toward highly effective lithium/sodium storage. *Chem Eng J* 2024;479:147914. DOI
125. He S, Wang Z, Qiu W, Zhao H, Lei Y. Effect of partial cation replacement on anode performance of sodium-ion batteries. *Batteries* 2024;10:44. DOI
126. Xu Y, Titirici M, Chen J, et al. 2023 roadmap for potassium-ion batteries. *J Phys Energy* 2023;5:021502. DOI
127. Marcus Y. Thermodynamic functions of transfer of single ions from water to nonaqueous and mixed solvents: part 3 - standard potentials of selected electrodes. *Pure Appl Chem* 1985;57:1129-32. DOI
128. Matsuda Y, Nakashima H, Morita M, Takasu Y. Behavior of some ions in mixed organic electrolytes of high energy density batteries. *J Electrochem Soc* 1981;128:2552-6. DOI
129. Bernhardt D, Reilly J. Mineral commodity summaries 2020. *US Geol Surv* 2020;1:116-7. DOI
130. Kim H, Kim JC, Bianchini M, Seo D, Rodriguez-Garcia J, Ceder G. Recent progress and perspective in electrode materials for K-ion batteries. *Adv Energy Mater* 2018;8:1702384. DOI
131. Wu X, Zhang W, Wu N, Pang S, He G, Ding Y. Exploration of nanoporous CuBi binary alloy for potassium storage. *Adv Funct Mater* 2020;30:2003838. DOI
132. Xie Y, Wang X, Zhang H, et al. Bimetallic alloy nanoparticles embedded in N-doped carbon-based as an anode for potassium-ion storage material. *J Electroanal Chem* 2024;959:118178. DOI
133. Zhang R, Luo Q, Gong J, et al. Multilevel spatial confinement of transition metal selenides porous microcubes for efficient and stable potassium storage. *J Colloid Interface Sci* 2023;644:10-8. DOI
134. Chen W, Hu K, Zheng H, et al. GeV_4S_8: a novel bimetallic sulfide for robust and fast potassium storage. *Small* 2024;20:e2311638. DOI
135. Ma Y, Ouyang Y, Liang H, et al. Heterostructured CoS_2/SnS_2 encapsulated in sulfur-doped carbon exhibiting high potassium ion storage capacity. *J Coll Interface Sci* 2024;661:671-80. DOI
136. Kim S, Kim TH, Park HK, Kang YC, Cho JS, Park GD. Aerosol-assisted synthesis of 3D hybridized reduced graphene oxide-carbon nanotube composite microsphere with cobalt-iron selenide nanocrystal as anode materials for potassium-ion batteries. *J Energy Stor* 2024;83:110683. DOI
137. Guo J, Wang L, Hu A, Zhang J, Xiao Z. 3D micro-flower structured $BiFeO_3$ constructing high energy efficiency/stability potassium ion batteries over wide temperature range. *Adv Funct Mater* 2024;34:2313300. DOI
138. Liang H, Wang X, Shi J, et al. Design of heterostructured hydrangea-like FeS_2/MoS_2 encapsulated in nitrogen-doped carbon as high-performance anode for potassium-ion capacitors. *J Colloid Interf Sci* 2024;664:96-106. DOI
139. Toro L, Moscardini E, Baldassari L, et al. A systematic review of battery recycling technologies: advances, challenges, and future prospects. *Energies* 2023;16:6571. DOI
140. Yu X, Li W, Gupta V, et al. Current challenges in efficient lithium-ion batteries' recycling: a perspective. *Glob Chall* 2022;6:2200099. DOI PubMed PMC
141. González YC, Alcaraz L, Alguacil FJ, González J, Barbosa L, López FA. Study of the carbochlorination process with CaC_{l2} and water leaching for the extraction of lithium from spent lithium-ion batteries. *Batteries* 2023;9:12. DOI
142. Porzio J, Scown CD. Life-cycle assessment considerations for batteries and battery materials. *Adv Energy Mater* 2021;11:2100771. DOI
143. Lorero I, Campo M, Del Rosario G, López FA, Prolongo SG. New manufacturing process of composites reinforced with ZnO nanoparticles recycled from alkaline batteries. *Polymers* 2020;12:1619. DOI PubMed PMC
144. Lorero I, Campo M, Arribas C, Prolongo MG, López FA, Prolongo SG. Epoxy composites reinforced with ZnO from waste alkaline batteries. *Materials* 2022;15:2842. DOI PubMed PMC
145. Alguacil FJ, Lopez FA. Separation iron(III)-manganese(II) via supported liquid membrane technology in the treatment of spent alkaline batteries. *Membranes* 2021;11:991. DOI PubMed PMC
146. Llamas-Orozco JA, Meng F, Walker GS, et al. Estimating the environmental impacts of global lithium-ion battery supply chain: a temporal, geographical, and technological perspective. *PNAS Nexus* 2023;2:pgad361. DOI PubMed PMC
147. Balali Y, Stegen S. Review of energy storage systems for vehicles based on technology, environmental impacts, and costs. *Renew Sustain Energy Rev* 2021;135:110185. DOI
148. Larcher D, Tarascon JM. Towards greener and more sustainable batteries for electrical energy storage. *Nat Chem* 2015;7:19-29. DOI PubMed
149. Helbig C, Hillenbrand M. Principles of a circular economy for batteries. In: Passerini S, Barelli L, Baumann M, Peters J, Weil M, editors. Emerging battery technologies to boost the clean energy transition. The materials research society series. Cham: Springe; 2024. DOI
150. Automated guided vehicle market size & share report 2030. Automated guided vehicle market trends. Available from: https://www.grandviewresearch.com/industry-analysis/automated-guided-vehicle-agv-market [Last accessed on 2 Aug 2024].
151. Tankou A, Bieker G, Hall D. Scaling up reuse and recycling of electric vehicle batteries: assessing challenges and policy approaches. In: Proc ICCT; 2023. pp. 1-138. Available from: https://theicct.org/wp-content/uploads/2023/02/recycling-electric-vehicle-batteries-feb-23.pdf [Last accessed on 2 Aug 2024].
152. Navarro RP, Seidel P, Lenz L, Kolk M, Krug A. European battery recycling: an emerging cross-industry convergence. In: Arthur D.

Litle; 2022. Available from:https://www.adlittle.mx/sites/default/files/viewpoints/ADL_European_battery_recycling.pdf [Last accessed on 2 Aug 2024].

153. Yu W, Guo Y, Shang Z, Zhang Y, Xu S. A review on comprehensive recycling of spent power lithium-ion battery in China. *eTransportation* 2022;11:100155. DOI
154. Yoo E, Lee U, Kelly JC, Wang M. Life-cycle analysis of battery metal recycling with lithium recovery from a spent lithium-ion battery. *Resour Conserv Recy* 2023;196:107040. DOI
155. Wang X, Guo W, Fu Y. High-entropy alloys: emerging materials for advanced functional applications. *J Mater Chem A* 2021;9:663-701. DOI
156. Tian H, Tian H, Wang S, et al. High-power lithium-selenium batteries enabled by atomic cobalt electrocatalyst in hollow carbon cathode. *Nat Commun* 2020;11:5025. DOI PubMed PMC
157. Wang R, Wang H, Zhao H, et al. Highly fluorinated co-solvent enabling ether electrolyte for high-voltage lithium ion batteries with graphite anode. *Energy Mater* 2023;3:300040. DOI
158. Lei K, Wang J, Chen C, et al. Recent progresses on alloy-based anodes for potassium-ion batteries. *Rare Met* 2020;39:989-1004. DOI
159. Jin C, Liu T, Sheng O, et al. Rejuvenating dead lithium supply in lithium metal anodes by iodine redox. *Nat Energy* 2021;6:378-87. DOI
160. Sun J, Liu C, Zheng P, et al. Exploring the potential of one-dimensional van der Waals material V_2PS_{10}/carbon composite: an anode design paradigm for lithium-ion batteries. *Next Mater* 2023;1:100053. DOI
161. Tian H, Liang J, Liu J. Nanoengineering carbon spheres as nanoreactors for sustainable energy applications. *Adv Mater* 2019;31:e1903886. DOI
162. Zhang Q, Wu L, Fan M, et al. A room temperature alloying strategy to enable commercial metal foil for efficient Li/Na storage and deposition. *Energy Stor Mater* 2021;34:708-15. DOI